Real-Time Identification of Wrist Kinematics via Sparsity-Promoting Extended Kalman Filter Based on Ellipsoidal Joint Formulation

Jiamin Wang, *Graduate Student Member, IEEE*, and Oumar R. Barry

Abstract*—*Objective: **This paper proposes a novel method for real-time wrist kinematics identification.** ***Method:*** **We design the wrist kinematics regression model following a novel ellipsoidal joint formulation, which features a quaternion-based rotation constraint and 2-dimensional Fourier linear combiners (FLC) to approximate the coupled rotations and translational displacements of the wrist. Extended Kalman Filter (EKF) is then implemented to update the model in real-time. However, unlike previous studies, here we introduce a sparsity-promoting feature in the model regression through the optimality of EKF by designing a smooth $\ell1$-minimization observation function. This is done to ensure the best identification of key parameters, and to improve the robustness of regression under noisy conditions.** ***Results:*** **Simulations employ multiple reference models to evaluate the performance of the proposed approach. Experiments are later carried out on motion data collected by a lab-developed wrist kinematics measurement tool. Both simulation and experiment show that the proposed approach can robustly identify the wrist kinematics in real-time.** ***Conclusion:*** **The findings confirm that the proposed regression model combined with the sparsity-promoting EKF is reliable in the real-time modeling of wrist kinematics.** ***Significance:*** **The proposed method can be applied to generic wrist kinematics modeling problems, and utilized in the control system of wearable wrist exoskeletons. The framework of the proposed method may also be applied to real-time identification of other joints for exoskeleton control.**

***Index Terms*—Wrist Kinematics, Ellipsoidal Joint, Real-time Model Regression, Fourier Linear Combiner, Quaternion-based Constraints, Extended Kalman Filter, $\ell1$-minimization**

NOMENCLATURE

The mathematical notations used are listed as following:

$\Vert\,\mathbf{Z}\,\Vert_n$	n-norm of a matrix $\mathbf{Z}$ ($n = 2$ if not specified)
$\bar{\mathbf{z}}$	Conjugation of quaternion $\mathbf{z}$ (4×1)
$\mathbf{c}_{m\times n}$	$m \times n$ matrix whose elements equal to $\mathbf{c} \in \mathbb{R}$ ($m,\ n$ fit with neighboring blocks if not specified)
$\mathbf{c}_m$	$m \times 1$ column vector whose elements equal to $\mathbf{c} \in \mathbb{R}$
$\mathbf{I}_n$	Identity matrix of dimension n ($m,\ n$ fit with neighboring blocks if not specified)
$\mathrm{diag}(\mathbf{z})$	Convert a m-dimensional vector $\mathbf{z}$ into a $m \times m$ diagonal matrix with elements from $\mathbf{z}$
$\mathrm{vec}(\mathbf{Z})$	Reshape a matrix $\mathbf{Z}$ elements into a column vector
$\mathbf{Z} > 0$	A square matrix $\mathbf{Z}$ is positive definite
$\mathbf{Z}^m$	Elemental-wise matrix $\mathbf{Z}$ to the power of m
$\mathbf{Z}^{-\mathrm{T}}$	Transposed inverse of $\mathbf{Z}$ (since $(\mathbf{Z}^{-1})^{\mathrm{T}} = (\mathbf{Z}^{\mathrm{T}})^{-1}$)
$\mathbf{Z}_1 * \mathbf{Z}_2$	Elemental-wise product of matrices $\mathbf{Z}_1$ and $\mathbf{Z}_2$
$\mathbf{z}_1 \times \mathbf{z}_2$	Product of quaternions $\mathbf{z}_1$ (4×1) and $\mathbf{z}_2$ (4×1)

The authors are with the Department of Mechanical Engineering, Virginia Tech, Blacksburg, VA, 24061, USA

Corresponding author: Oumar R. Barry (Email: obarry@vt.edu)

I. INTRODUCTION

The wrist is pivotal to humans in performing manipulation tasks. The wrist possesses multiple coupled degrees of freedom (DOF), whose primary motions are generalized as flexion-extension (FE) and radial-ulnar deviation (RUD). The two motions are largely generated by the radiocarpal joint and midcarpal joint [1], [2]. The behaviors of these two joints are distinctive, especially when the wrist is at extreme postures [3]. Due to the complex kinematics introduced by the biomechanics of wrist skeletal system, the approximate rotation axes of FE and RUD can change translationally and rotationally during wrist movements [4], [5].

The wrist biomechanics has been extensively investigated, which includes assessing wrist kinematics from experimental data [6], [5], [7], [8], [9], the coupling between wrist motions [10], and dynamical properties of the wrist [11], [12]. In these studies, the wrist kinematics is often approximated by sequential rotational joints, where multiple rotations take place one after another [6], [7], [10], [11], [12], [13], [14]. These models are uniquely defined by their rotation sequences. As examples, the first-FE-then-RUD model [10], [13] is different from the first-RUD-then-FE model [9]. The uniqueness of these models can manifest significantly at extreme FE and RUD positions. Also, translational motions in the wrist are neglected in some models, which may fail to describe the coupling between wrist translations and rotations [15].

An accurate wrist kinematic model can be crucial to the development of rehabilitation robotic devices [16], [17], [18], [19], [20]. We are developing the Tremor Alleviating Wrist Exoskeleton (TAWE) [16] for people suffering from pathological tremors (e.g., Parkinson's Diseases [21], Essential Tremor [22]). As shown in Fig. 1, TAWE is designed to suppress

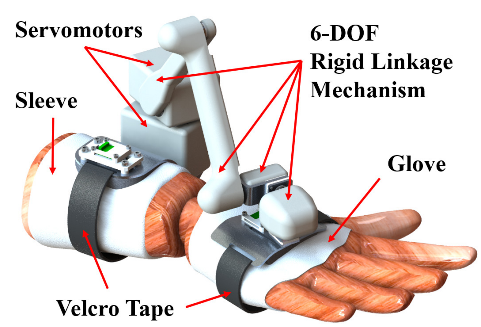

Fig. 1. The CAD design of the Tremor Alleviating Wrist Exoskeleton [16].

This article has been accepted for publication in a future issue of this journal, but has not been fully edited. Content may change prior to final publication. Citation information: DOI 10.1109/TBME.2021.3111878, IEEE Transactions on Biomedical Engineering

tremors in both FE and RUD motions via an actuated 6-DOF rigid linkage mechanism that forms a closed kinematic chain with the wrist, whose information is crucial to the control system of TAWE [16]. Since TAWE is wearable through sleeves, gloves, and Velcro tapes, the closed kinematic chain parameters may slowly change over time due to small shifts in wearing locations. This motivates us to explore the regression of wrist kinematics with real-time adaptability. In earlier studies [7], [8], [9], however, the wrist kinematics modeling were performed on offline motion data.

For general real-time signal regressions, Kalman Filters are frequently used as optimizers to update model parameters online [23], [24]. Also, uncertain signal features can be approximated by various model structures such as autoregressive models, Fourier linear combiners (FLC), and support vector machines [25], [26], [27], [28]. These models, however, can introduce significantly more parameters, which increases model complexity and may lead to overfitting. This challenge can be resolved with sparsity-promoting technique such as $\ell 1$-minimization [29], [30], which can reduce redundant parameters without significant loss of regression accuracy.

This paper presents, for the first time, a real-time wrist kinematics identification (WKI) approach based on a novel ellipsoidal joint formulation. The proposed method applies to generic wrist kinematics modeling problems. The ellipsoidal joint, unlike sequential rotational joints, employs a quaternion-based constraint to characterize the constrained 3D rotation of the wrist (i.e, FE and RUD motions) [31]. An advantage of the quaternion-based constraint is that, with specific modifications of its expression, the resulting constrained wrist rotations are identical to the corresponding sequential rotations. The ellipsoidal joint also introduces geometric constraints to couple translational motions with FE and RUD motions [32], which primarily resembles the radiocarpal joint translations.

Based on the ellipsoidal joint formulation, we further generalize the WKI regression model by using 2D Fourier linear combiners (FLC) to approximate uncertain model features. Extended Kalman Filter (EKF) is then implemented for the real-time nonlinear regression. We also apply sparsity-promoting features via the optimality of EKF by designing smooth observation functions that realize $\ell 1$-minimization. The sparsity-promoting EKF (SP-EKF) ensures the correct identification of primary wrist kinematic parameters, and can improve the robustness towards noise. We compare the WKI performances with different algorithm configurations through simulations that employ various reference models. A lab-developed wrist kinematics measurement tool (WKMT) is later used to collect data for experimental validations.

The rest of the paper is arranged as follows. In Section II, the ellipsoidal joint formulation and the WKI regression model are presented. Section III introduces the WKMT design and discusses the theories of the SP-EKF. Numerical simulations are presented in Section IV to validate analytical findings and study the performance of WKI algorithm. Section V discusses experimental results of WKI algorithm based on wrist motion data collected by WKMT. Finally, Section VI summarizes the findings and proposes future works.

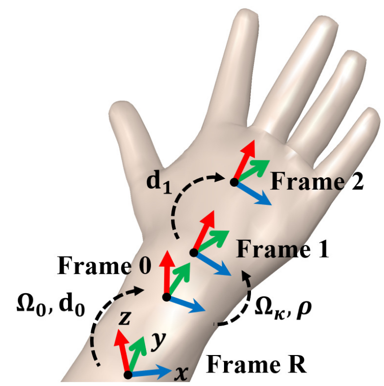

Fig. 2. The wrist kinematic chain in a right human forearm, where the Frame R is located at the forearm, Frame 2 is located at the hand. The wrist motions take place between the intermediate frames, i.e., Frame 0 and Frame 1.

TABLE I
PROPERTIES OF TRANSFORMATIONS BETWEEN COORDINATE FRAMES FROM THE WRIST KINEMATIC SYSTEM SHOWN IN FIG. 2.

From	To	Translation ($\mathbb{R}^3$)	Rotation ($\mathbb{R}^{3\times3}$)
R	0	$\mathbf{d}_0$	$\boldsymbol{\Omega}_0(\boldsymbol{\xi}_0)$
0	1	$\boldsymbol{\rho}$	$\boldsymbol{\Omega}_\kappa(\boldsymbol{\kappa})$
1	2	$\mathbf{d}_1$	$\mathbf{I}_3$

II. Modeling of the Wrist Kinematics

A right human forearm is presented in Fig. 2, where the reference frame (Frame R) is located at the forearm, and Frame 2 is located at the hand. The wrist motions take place between the intermediate frames, i.e., Frame 0 and Frame 1. With respect to Frame 0, FE is defined along x direction, RUD is defined along z direction, and y direction is approximately the forearm pronation-supination (PS) direction.

The transformations between frames are shown in Table I, where $\mathbf{d}_0,\ \mathbf{d}_1 \in \mathbb{R}^3$ are fixed translational displacements. The rotation between two frames can be represented by a unique rotation matrix $\boldsymbol{\Omega} \in \mathbb{R}^{3\times3}$, which satisfies $\boldsymbol{\Omega}^{-1} = \boldsymbol{\Omega}^{\mathrm{T}}$. The coordinate frames are defined so that rotation $\boldsymbol{\Omega}_0$ between Frame R and Frame 0 is fixed, which can also be equivalently represented by a unit quaternion vector $\boldsymbol{\xi}_0 \in \mathbb{R}^4$. Also, we assume no rotation between Frame 1 and Frame 2. The wrist motions are characterized by translational displacement $\boldsymbol{\rho} = [\rho_x,\ \rho_y,\ \rho_z]^{\mathrm{T}}$, and yaw-pitch-roll (intrinsic z-y-x) Euler angles $\boldsymbol{\kappa} = [\kappa_x,\ \kappa_y,\ \kappa_z]^{\mathrm{T}}$ that lead to the rotation matrix $\boldsymbol{\Omega}_\kappa$

$$\boldsymbol{\Omega}_\kappa(\boldsymbol{\kappa}) = \boldsymbol{\Omega}_z(\kappa_z)\boldsymbol{\Omega}_y(\kappa_y)\boldsymbol{\Omega}_x(\kappa_x) \tag{1}$$

where $\boldsymbol{\Omega}_i$ is the rotation matrix along i axis (for $i = x,\ y,\ z$).

In this paper, the generalized coordinate vector for the wrist motions is defined as $\mathbf{q} = [q_1,\ q_2]^{\mathrm{T}} = [\kappa_z,\ \kappa_x]^{\mathrm{T}}$, where $q_1 > 0$ is radial deviation, $q_1 < 0$ is ulnar deviation, $q_2 > 0$ is extension, and $q_2 < 0$ is flexion. Since FE and RUD motions are the two main wrist DOFs, we assume that the rotation κ_y on PS direction is constrained by $\mathbf{q}$, and the translation $\boldsymbol{\rho}$ is coupled with $\boldsymbol{\kappa}$. Hence, the FE and RUD rotation axes can shift translational with $\boldsymbol{\rho}$ and rotationally with κ_y. Following these two assumptions, we propose the model interpretation of wrist kinematics through ellipsoidal joint formulation [31].

This article has been accepted for publication in a future issue of this journal, but has not been fully edited. Content may change prior to final publication. Citation information: DOI 10.1109/TBME.2021.3111878, IEEE Transactions on Biomedical Engineering

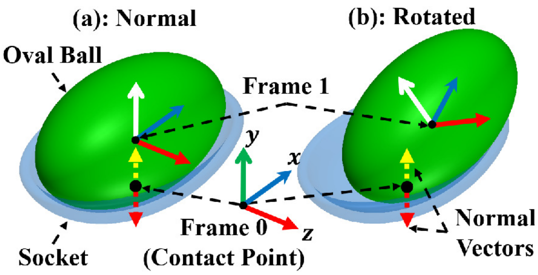

Fig. 3. Illustration of an ellipsoidal joint, where the origin of Frame 0 is located at the bottom of the ellipsoidal socket, which is also the contact point between the oval ball and the ellipsoidal socket, and Frame 1 is located at the center of the oval ball. The normal vectors are respectively perpendicular to the oval ball and ellipsoidal socket surfaces at the contact point. The y axis of Frame 0 is colinear with the normal vectors.

A. Quaternion-Based Constraint on Wrist Rotation

An ellipsoidal joint is illustrated in Fig. 3, which is similar to a ball joint except that the rotation of oval ball can be constrained by the ellipsoidal socket. Following this idea, we introduce the quaternion-based constraint to bind the wrist rotation κ_y on forearm PS direction to $\mathbf{q}$ (i.e., FE and RUD). The basic version of the constraint is written as

$$r_\kappa(\boldsymbol{\kappa}) = \begin{bmatrix}1 & \mathbf{0}_{1\times 3}\end{bmatrix}\left(\begin{bmatrix}\mathbf{0}_{1\times 2} & 1 & 0\end{bmatrix}^{\mathrm{T}} \times \boldsymbol{\xi}_\kappa(\boldsymbol{\kappa})\right) = 0 \tag{2}$$

where $\boldsymbol{\xi}_\kappa \in \mathbb{R}^4$ is the quaternion vector that represents the rotation $\boldsymbol{\Omega}_\kappa$, which can be converted from $\boldsymbol{\kappa}$. The effect of r_κ can be interpreted from the 3D axis-angle perspective [33], i.e., the 3D rotation vector of $\boldsymbol{\Omega}_\kappa$ is constrained on the x-z plane of Frame 0. The explicit expression of Eq. (2) is

$$\begin{aligned} r_\kappa(\boldsymbol{\kappa}) = &-\cos(\kappa_y/2)\sin(\kappa_x/2)\sin(\kappa_z/2)\\ &-\cos(\kappa_x/2)\cos(\kappa_z/2)\sin(\kappa_y/2) \end{aligned} \tag{3}$$

which leads to

$$\kappa_y = 2\arctan\left(\frac{-\sin(\kappa_x/2)\sin(\kappa_z/2)}{\cos(\kappa_x/2)\cos(\kappa_z/2)}\right) \tag{4}$$

This shows that the constraint does not set $\kappa_y = 0$, which also indicates that κ_z and κ_x are non-orthogonal rotations.

As previously mentioned, the basic quaternion constraint in Eq. (2) can be modified with additional specific terms so that the wrist rotation is identical to the sequential rotation joints from previous studies. Here we present three examples.

The first example is the first-RUD-then-FE orthogonal joint model [9], where the constraint simply set $\kappa_z = 0$ so that

$$\boldsymbol{\Omega}_{\kappa,1}(\boldsymbol{\kappa}) = \boldsymbol{\Omega}_z(\kappa_z)\boldsymbol{\Omega}_x(\kappa_x) \tag{5}$$

If the quaternion-based constraint is modified into

$$r_{\kappa,1}(\boldsymbol{\kappa}) = r_\kappa + \sin(\kappa_x/2)\sin(\kappa_z/2) = 0 \tag{6}$$

then we obtain the constrained rotation $\boldsymbol{\Omega}_\kappa$ identical to $\boldsymbol{\Omega}_{\kappa,1}$.

For the first-FE-then-RUD orthogonal joint [10], [13], we define the intrinsic x-y-z Euler angles $\boldsymbol{\phi} = [\phi_x,\ \phi_y,\ \phi_z]^{\mathrm{T}}$ that present the same rotation $\boldsymbol{\Omega}_\kappa$ through

$$\boldsymbol{\Omega}_\kappa(\boldsymbol{\kappa}) = \boldsymbol{\Omega}_\phi(\boldsymbol{\phi}) = \boldsymbol{\Omega}_x(\phi_x)\boldsymbol{\Omega}_y(\phi_y)\boldsymbol{\Omega}_z(\phi_z) \tag{7}$$

Similar to the previous case, the first-FE-then-RUD orthogonal joint constrains ϕ_y to 0, and adopts ϕ_x and ϕ_z respectively as the generalized coordinates for FE and RUD. This leads to

$$\boldsymbol{\Omega}_{\kappa,2}(\boldsymbol{\kappa}) = \boldsymbol{\Omega}_x(\phi_x)\boldsymbol{\Omega}_z(\phi_z) \tag{8}$$

The equivalent quaternion-based constraint that yields the rotation identical to $\boldsymbol{\Omega}_{\kappa,2}$ can be written as

$$r_{\kappa,2}(\boldsymbol{\kappa}) = r_\kappa - \sin(\phi_x/2)\sin(\phi_z/2) = 0 \tag{9}$$

Finally, some studies model the wrist rotation with two serially connected orthogonal joints, which respectively approximates the radiocarpal and midcarpal joints [34], [35]. For instance, we define the intrinsic x-y-z Euler angles $\boldsymbol{\psi} = [\psi_x,\ \psi_y,\ \psi_z]^{\mathrm{T}}$ that satisfies

$$\boldsymbol{\Omega}_\psi(\boldsymbol{\psi}) = \boldsymbol{\Omega}_x(\psi_x)\boldsymbol{\Omega}_y(\psi_y)\boldsymbol{\Omega}_z(\psi_z) \tag{10a}$$
$$\boldsymbol{\Omega}_\kappa(\boldsymbol{\kappa}) = \boldsymbol{\Omega}_\psi(\boldsymbol{\psi})\boldsymbol{\Omega}_\psi(\boldsymbol{\psi}) \tag{10b}$$

where $\boldsymbol{\Omega}_\psi$ is equivalent of a half-rotation of $\boldsymbol{\Omega}_\kappa$. By choosing ψ_x and ψ_z respectively as the generalized coordinates for FE and RUD, and enforcing constraint $\psi_y = 0$, the FE-RUD-FE-RUD joint can be written as [34], [35]

$$\boldsymbol{\Omega}_{\kappa,3}(\boldsymbol{\kappa}) = \boldsymbol{\Omega}_x(\psi_x)\boldsymbol{\Omega}_z(\psi_z)\boldsymbol{\Omega}_x(\psi_x)\boldsymbol{\Omega}_z(\psi_z) \tag{11}$$

Hence, the modified quaternion-based constraint designed as

$$r_{\kappa,3}(\boldsymbol{\kappa}) = r_\kappa - \sin(\psi_x)\sin(\psi_z)/2 = 0 \tag{12}$$

yields $\boldsymbol{\Omega}_\kappa$ as the same rotation to $\boldsymbol{\Omega}_{\kappa,3}$

Note that in Eq. (8) and Eq. (11), both $\boldsymbol{\phi}$ and $\boldsymbol{\psi}$ can be represented by complicated symbolic expressions of $\boldsymbol{\kappa}$ through conversion respectively based on Eq. (7) and Eq. (10). Also, provided that $\kappa_y \approx 0$, when κ_x or κ_z approaches zero, we can approximately obtain

$$\begin{aligned} \sin(\kappa_x/2)\sin(\kappa_z/2) &\approx -\sin(\phi_x/2)\sin(\phi_z/2)\\ &\approx -2\sin(\psi_x)\sin(\psi_z) \end{aligned} \tag{13}$$

with $\boldsymbol{\phi}$ and $\boldsymbol{\psi}$ that satisfy $\boldsymbol{\Omega}_\kappa(\boldsymbol{\kappa}) = \boldsymbol{\Omega}_\phi(\boldsymbol{\phi}) = \boldsymbol{\Omega}_\psi(\boldsymbol{\psi})\boldsymbol{\Omega}_\psi(\boldsymbol{\psi})$. On the other hand, when $\mathbf{q}$ is far from zeros, having $\boldsymbol{\kappa} = \boldsymbol{\phi} = 2\boldsymbol{\psi}$ can lead to significant differences among $\boldsymbol{\Omega}_\kappa$, $\boldsymbol{\Omega}_\phi$ and $\boldsymbol{\Omega}_\psi$.

B. Ellipsoid-Based Translational Constraints

The translational motions in the ellipsoidal joint from Fig. 3 is coupled with rotation $\boldsymbol{\Omega}_\kappa$. For this case, we define $\boldsymbol{\rho}_0 \in \mathbb{R}^3$ as a solution for $\boldsymbol{\rho}$. Unlike a ball joint, the ellipsoidal socket and oval ball are not always concentric. By assuming that the oval ball and ellipsoidal socket surfaces are tangent and always in contact, we define the origins of Frame 0 and Frame 1 at the contact point and the center of oval ball, respectively. This leads to a constraint based on the ellipsoid equation [32]

$$r_{\rho,1}(\boldsymbol{\kappa}, \boldsymbol{\rho}_0) = \boldsymbol{\rho}_0^{\mathrm{T}}\boldsymbol{\Omega}_\kappa \mathrm{diag}\left(\begin{bmatrix}c_{\rho,1}^2 & c_{\rho,2}^2 & c_{\rho,3}^2\end{bmatrix}\right)^{-1}\boldsymbol{\Omega}_\kappa^{\mathrm{T}}\boldsymbol{\rho}_0 - 1 = 0 \tag{14}$$

where $\mathbf{c}_\rho = [c_{\rho,1},\ c_{\rho,2},\ c_{\rho,3}] > 0$ contains the radii of oval ball. It is also assumed that, the normal vector of the oval ball surface at contact point is normal to the socket surface. The normal vector of oval ball surface can be calculated by

$$\mathbf{a}_n(\boldsymbol{\kappa}, \boldsymbol{\rho}_0) = 2\ \mathrm{diag}\left(\begin{bmatrix}c_{\rho,1}^2 & c_{\rho,2}^2 & c_{\rho,3}^2\end{bmatrix}\right)^{-1}\boldsymbol{\Omega}_\kappa^{\mathrm{T}}\boldsymbol{\rho}_0 \tag{15}$$

Hence, a second set of translational constraints is formed

$$\mathbf{r}_{\rho,2}(\boldsymbol{\kappa},\boldsymbol{\rho}_0)=\begin{bmatrix}1 & 0 & 0\\ 0 & 0 & 1\end{bmatrix}\boldsymbol{\Omega}_\kappa\mathbf{a}_n=\mathbf{0} \tag{16}$$

which ensures that the y axis in Frame 0 is colinear to the normal vector. This constraint also fixes the contact point at the bottom of the socket. Thus, the oval ball cannot be lifted from the socket. The explicit solution of $\boldsymbol{\rho}_0$ as expressions of $\boldsymbol{\kappa}$ solved from Eq. (14, 16) are presented in Appendix A. Note that when $c_{\rho,1}=c_{\rho,2}=c_{\rho,3}$, we can obtain a regular ball joint and a constant solution $\boldsymbol{\rho}_0=[0,\ c_{\rho,2},\ 0]$.

It is also important to note that $\boldsymbol{\rho}_0$ primarily approximates the potential translations in the radiocarpal joint, where the proximal row of carpal bones rolls in the cavity formed by the radius bone and the articular disk [4]. The translation in midcarpal joint caused by the gliding between the proximal and distal rows of carpal bones is not considered in $\boldsymbol{\rho}_0$.

C. General Model for Wrist Kinematics Identification

The wrist kinematics in real life can be much more complicated than the proposed ellipsoidal joint model. Also, the expressions of $\boldsymbol{\rho}_0$ in Eq. (A-2) is not numerically robust for regression, since $\mathbf{c}_\rho$ approaching zeros will result in singularities. Therefore, a general regression model is designed for the wrist kinematics identification (WKI) algorithm by referencing the proposed ellipsoidal joint model.

To begin with, the transformation between Frame 2 and Frame R can be calculated from Table I as

$$\mathbf{d}_m=\mathbf{d}_0+\boldsymbol{\Omega}_0\boldsymbol{\rho}+\boldsymbol{\Omega}_0\boldsymbol{\Omega}_\kappa\mathbf{d}_1 \tag{17a}$$
$$\boldsymbol{\xi}_m=\boldsymbol{\xi}_0\times\boldsymbol{\xi}_\kappa \tag{17b}$$

where $\mathbf{d}_m\in\mathbb{R}^3$ is the translational displacement, and $\boldsymbol{\xi}_m\in\mathbb{R}^4$ is the unit quaternion vector that represents the rotation $\boldsymbol{\Omega}_m=\boldsymbol{\Omega}_0\boldsymbol{\Omega}_\kappa$. In practice, we can only measure $\mathbf{d}_m$ and $\boldsymbol{\xi}_m$, and $\boldsymbol{\xi}_0$, $\mathbf{d}_0$, and $\mathbf{d}_1$ are unknown fixed parameters that need to be identified. Also, $\boldsymbol{\kappa}$ and its quaternion $\boldsymbol{\xi}_\kappa$ are not directly available but instead estimated through

$$\boldsymbol{\xi}_\kappa=\bar{\boldsymbol{\xi}}_0\times\boldsymbol{\xi}_m \tag{18}$$

As previously discussed, since FE (κ_x) and RUD (κ_z) are the main DOFs of the wrist, both κ_y and $\boldsymbol{\rho}$ are assumed to be constrained by $\mathbf{q}$. Also, the range of motion of the wrist indicate that these movements are bounded within the FE-RUD domain. Therefore, we introduce the Fourier linear combiners (FLC) to approximate the nonlinear wrist kinematics that are difficult to model [26], [27]. The FLC is designed based on the 2D Fourier series expansion with respect to $\mathbf{q}$ in the FE-RUD domain. The 2D FLC vector $\mathbf{a}_{f,n}$ can be obtained from

$$\begin{aligned}\mathbf{a}_{f,n,0}&=\mathrm{vec}\left(\begin{bmatrix}1 & \mathbf{a}_{f,n,s,1} & \mathbf{a}_{f,n,c,1}\end{bmatrix}^{\mathrm{T}}\begin{bmatrix}1 & \mathbf{a}_{f,n,s,2} & \mathbf{a}_{f,n,c,2}\end{bmatrix}\right)\\ &=\begin{bmatrix}1 & \mathbf{a}_{f,n}^{\mathrm{T}}\end{bmatrix}^{\mathrm{T}}\end{aligned} \tag{19}$$

based on the following vectors that contain sinusoidal terms

$$\mathbf{a}_{f,n,s,1}=\begin{bmatrix}\sin(q_1) & \sin(2q_1) & \cdots & \sin(nq_1)\end{bmatrix} \tag{20a}$$
$$\mathbf{a}_{f,n,s,2}=\begin{bmatrix}\sin(q_2) & \sin(2q_2) & \cdots & \sin(nq_2)\end{bmatrix} \tag{20b}$$
$$\mathbf{a}_{f,n,c,1}=\begin{bmatrix}\cos(q_1) & \cos(2q_1) & \cdots & \cos(nq_1)\end{bmatrix} \tag{20c}$$
$$\mathbf{a}_{f,n,c,2}=\begin{bmatrix}\cos(q_2) & \cos(2q_2) & \cdots & \cos(nq_2)\end{bmatrix} \tag{20d}$$

The Fourier series expansion order n is selected based on the trade-off between model complexity and approximation accuracy. In this paper, we select $n=2$. Hence, we approximate the nonlinear and complicated real wrist translational displacement $\boldsymbol{\rho}$ through a solution $\boldsymbol{\rho}_w$ designed as

$$\boldsymbol{\rho}_w=\boldsymbol{\Omega}_0^{\mathrm{T}}(\mathbf{D}_l\mathbf{q}+\mathbf{D}_f\mathbf{a}_{f,n}) \tag{21}$$

where $\mathbf{D}_l\in\mathbb{R}^{3\times 2}$ contains parameters for the $\mathbf{q}$-affine linear regression term; and $\mathbf{D}_f\in\mathbb{R}^{3\times((2n+1)^2-1)}$ contains amplitude parameters for the 2D FLC term. Adopting $\boldsymbol{\rho}_w$ leads to the general regression model for wrist translational displacement

$$\mathbf{d}_w(\boldsymbol{\kappa})=\mathbf{d}_0+\boldsymbol{\Omega}_0\boldsymbol{\Omega}_\kappa\mathbf{d}_1+\mathbf{D}_l\mathbf{q}+\mathbf{D}_f\mathbf{a}_{f,n}\approx\mathbf{d}_m \tag{22}$$

The regression model for wrist rotational constraint is designed by modifying of the basic quaternion-based constraint from Eq. (2), which can be written as

$$r_w(\boldsymbol{\kappa})=r_\kappa(\boldsymbol{\kappa})+c_\xi\sin(\kappa_x/2)\sin(\kappa_z/2)+\mathbf{c}_f\mathbf{a}_{f,n}\approx 0 \tag{23}$$

where $c_{\boldsymbol{\xi}}$ is an unknown real parameter; and $\mathbf{c}_f\in\mathbb{R}^{(2n+1)^2-1}$ contains amplitude parameters for the 2D FLC term. Based on the approximation from Eq. (13), $c_{\boldsymbol{\xi}}$ can classify the characteristics of identified wrist rotation. Specifically, $c_{\boldsymbol{\xi}}\approx 1$ indicates similarity to the first-RUD-then-FE joint according to Eq. (6); $c_{\boldsymbol{\xi}}\approx -1$ suggests similarity to the first-FE-then-RUD joint based on Eq. (9); and $c_{\boldsymbol{\xi}}\approx -0.5$ indicates similarity to the FE-RUD-FE-RUD joint according to Eq. (12).

The WKI regression models in Eqs. (22, 23) contain many unknown translational and rotational parameters, which are collected in the parameter vector $\mathbf{p}$ written as

$$\mathbf{p}=\begin{bmatrix}\boldsymbol{\xi}_0^{\mathrm{T}} & c_\xi & \mathbf{c}_f & \mathbf{d}_0^{\mathrm{T}} & \mathbf{d}_1^{\mathrm{T}} & \mathrm{vec}^{\mathrm{T}}(\mathbf{D}_l) & \mathrm{vec}^{\mathrm{T}}(\mathbf{D}_f)\end{bmatrix}^{\mathrm{T}} \tag{24}$$

where $\boldsymbol{\xi}_0$, c_ξ, $\mathbf{d}_0$, and $\mathbf{d}_1$ are the primary wrist kinematic parameters. In the next section, we discuss the identification of $\mathbf{p}$ via sparsity-promoting extended Kalman filter.

III. Real-Time Wrist Kinematics Identification

A. The Extended Kalman Filter Process

To solve the real-time parameter identification problem, the extended Kalman filter (EKF) is employed [23]. The nonlinear discrete-time model for EKF can be generalized as

$$\mathbf{x}_k=\mathbf{f}(t,\mathbf{x}_{k-1},\mathbf{u}_k,\mathbf{v}_k) \tag{25a}$$
$$\mathbf{y}_k=\mathbf{h}(t,\mathbf{x}_k,\mathbf{u}_k,\mathbf{w}_k) \tag{25b}$$

where $t=k/c_{f,s}$ is the time, with k as discrete time, and $c_{f,s}$ as the sampling rate of the discrete time system; $\mathbf{x}_k$ is the internal state vector at discrete time k (the same notation with k applies for the other terms); $\mathbf{u}$ is the input; $\mathbf{v}$ is the process noise; $\mathbf{y}$ is the observation; $\mathbf{w}$ is the observation noise; $f(t,\mathbf{x}_{k-1},\mathbf{u}_k,\mathbf{v}_k)$ is the model process function; and $h(t,\mathbf{x}_k,\mathbf{u}_k,\mathbf{w}_k)$ is the observation function.

In this study, it is assumed that both $\mathbf{v}$ and $\mathbf{w}$ are independently stochastic under Gaussian distributions with zero means. The augmented state vector $\mathbf{z}_k$ and its covariance matrix $\mathbf{P}_a=\mathbf{P}_a^T>0$ can be constructed as [36]

$$\mathbf{z}_k=\begin{bmatrix}\mathbf{x}_k\\ \mathbf{v}_k\\ \mathbf{w}_k\end{bmatrix};\quad \mathbf{P}_{a,k}=\begin{bmatrix}\mathbf{P}_{xx,k} & \mathbf{0} & \mathbf{0}\\ \mathbf{0} & \mathbf{Q} & \mathbf{0}\\ \mathbf{0} & \mathbf{0} & \mathbf{R}\end{bmatrix} \tag{26}$$

whose elements are initialized as

$$E(\mathbf{v}\mathbf{v}^{\mathrm{T}}) = \mathbf{Q}; \quad E(\mathbf{w}\mathbf{w}^{\mathrm{T}}) = \mathbf{R} \tag{27a}$$

$$E(\mathbf{x}_0) = \bar{\mathbf{x}}_0; \quad E((\mathbf{x}_0 - \bar{\mathbf{x}}_0)(\mathbf{x}_0 - \bar{\mathbf{x}}_0)^{\mathrm{T}}) = \mathbf{P}_{xx,0} \tag{27b}$$

where $\mathbf{Q}$ and $\mathbf{R}$ are respectively the covariance of $\mathbf{v}$ and $\mathbf{w}$; and $\bar{\mathbf{x}}$ and $\mathbf{P}_{xx} = \mathbf{P}_{xx}^{\mathrm{T}}$ are respectively the mean/posteriori state estimate and state covariance.

EKF is a nonlinear extension of the standard Kalman filter which estimates the mean and covariance based on the system linearization at $\bar{\mathbf{x}}$, which is equivalent to the mean of the current state. The predict process of EKF can be written as

$$\hat{\mathbf{x}}_k = \mathbf{f}(t, \bar{\mathbf{x}}_{k-1}, \mathbf{u}_k, \mathbf{0}); \quad \hat{\mathbf{y}}_k = \mathbf{h}(t, \hat{\mathbf{x}}_k, \mathbf{u}_k, \mathbf{0}); \tag{28a}$$

$$\hat{\mathbf{P}}_{xx,k} = \mathbf{F}_{x,k}\mathbf{P}_{xx,k-1}\mathbf{F}_{x,k}^{\mathrm{T}} + \mathbf{F}_{v,k}\mathbf{Q}\mathbf{F}_{v,k}^{\mathrm{T}} \tag{28b}$$

$$\hat{\mathbf{P}}_{yy,k} = \mathbf{H}_{x,k}\hat{\mathbf{P}}_{xx,k}\mathbf{H}_{x,k}^{\mathrm{T}} + \mathbf{H}_{w,k}\mathbf{R}\mathbf{H}_{w,k}^{\mathrm{T}}; \tag{28c}$$

$$\hat{\mathbf{P}}_{xy,k} = \hat{\mathbf{P}}_{xx,k}\mathbf{H}_{x,k}^{\mathrm{T}} \tag{28d}$$

and the update process can be presented as

$$\boldsymbol{\epsilon}_k = \mathbf{y}_k - \hat{\mathbf{y}}_k; \quad \mathbf{G}_k = \hat{\mathbf{P}}_{xy,k}\hat{\mathbf{P}}_{yy,k}^{-1} \tag{29a}$$

$$\boldsymbol{\delta}_k = \bar{\mathbf{x}}_k - \hat{\mathbf{x}}_k = \mathbf{G}_k\boldsymbol{\epsilon}_k \tag{29b}$$

$$\mathbf{P}_{xx,k} = \hat{\mathbf{P}}_{xx,k} - \mathbf{G}_k\hat{\mathbf{P}}_{yy,k}\mathbf{G}_k^{\mathrm{T}} \tag{29c}$$

where $\hat{\mathbf{x}}$ is the priori estimated state, $\hat{\mathbf{y}}$ is the priori estimated observation; $\boldsymbol{\delta}$ is the update step between the posteriori mean $\bar{\mathbf{x}}$ and priori mean $\hat{\mathbf{x}}$; $\boldsymbol{\epsilon}$ is the error between the measured observation $\mathbf{y}$ and estimated observation $\hat{\mathbf{y}}$; $\hat{\mathbf{P}}_{yy} = \hat{\mathbf{P}}_{yy}^{\mathrm{T}} > 0$ is the priori estimated covariance of $\mathbf{y}$; $\hat{\mathbf{P}}_{xy} = \hat{\mathbf{P}}_{yx}^{\mathrm{T}}$ is the priori estimated cross covariance between $\mathbf{x}$ and $\mathbf{y}$; $\mathbf{G}$ is the approximated optimal Kalman gain; and the Jacobian matrices $\mathbf{F}$ and $\mathbf{H}$ are defined as

$$\mathbf{F}_{x,k} = \partial\mathbf{f}(t, \bar{\mathbf{x}}_{k-1}, \mathbf{u}_k, \mathbf{v}_k)/\partial\bar{\mathbf{x}}_{k-1}; \tag{30a}$$

$$\mathbf{F}_{v,k} = \partial\mathbf{f}(t, \bar{\mathbf{x}}_{k-1}, \mathbf{u}_k, \mathbf{v}_k)/\partial\mathbf{v}_k \tag{30b}$$

$$\mathbf{H}_{x,k} = \partial\mathbf{h}(t, \hat{\mathbf{x}}_k, \mathbf{u}_k, \mathbf{w}_k)/\partial\hat{\mathbf{x}}_k; \tag{30c}$$

$$\mathbf{H}_{w,k} = \partial\mathbf{h}(t, \hat{\mathbf{x}}_k, \mathbf{u}_k, \mathbf{w}_k)/\partial\mathbf{w}_k \tag{30d}$$

Previous studies have demonstrated that Kalman filters can also be used to formulate dynamic (real-time) optimizer [24], [29], [30]. For each propagation, the update $\boldsymbol{\delta}$ in Eq. (29b) carried out with gain and error is a step towards minimizing the cost function

$$\begin{aligned}\mathcal{J}_0(\bar{\mathbf{x}}_k) = &\big((\mathbf{y}_k - \mathbf{h}(t, \bar{\mathbf{x}}_k, \mathbf{u}_k, \mathbf{0}))^{\mathrm{T}}(\hat{\mathbf{P}}_{yy,k} - \hat{\mathbf{P}}_{xy,k}^{\mathrm{T}}\hat{\mathbf{P}}_{xx,k}^{-1} \\ &\hat{\mathbf{P}}_{xy,k})^{-1}(\mathbf{y}_k - \mathbf{h}(t, \bar{\mathbf{x}}_k, \mathbf{u}_k, \mathbf{0}))\big) \\ &+ (\bar{\mathbf{x}}_k - \hat{\mathbf{x}}_k)^T\hat{\mathbf{P}}_{xx,k}^{-1}(\bar{\mathbf{x}}_k - \hat{\mathbf{x}}_k)\end{aligned} \tag{31}$$

by optimizing the value of $\bar{\mathbf{x}}_k = \mathrm{argmin}(\mathcal{J}_0)$. This is later used to introduce sparsity-promoting features into the EKF process.

B. The 6-DOF Wrist Motion Measurement Tool

The wearable wrist kinematics measurement tool (WKMT) is developed to collect motion data from the user for identification. As shown in Fig. 4, WKMT features a 6-DOF rigid linkage mechanism connecting Frame R and Frame 2, which supports any translations and rotations between the two frames within its reachable workspace. Hence, WKMT allows unconstrained and natural wrist movements.

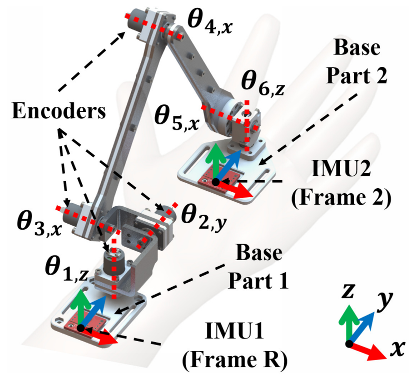

Fig. 4. The design of WKMT and its approximate location on the right human forearm. The two IMUs on the base parts measures the rotations of Frame R and Frame 2, respectively. The joints θ are marked around their rotation axes (red dot lines), which are labeled with their sequence numbers and rotation axes in their local frames. Encoders are installed on the first four joints.

WKMT can adopt various sensor configurations to fully measure the displacement $\mathbf{d}_m$ and rotation $\boldsymbol{\xi}_m$ between Frame 2 and Frame R as introduced in Eq. (17), so that the input $\mathbf{u}_1$ for the WKI process is defined as

$$\mathbf{u}_1 = \begin{bmatrix}\boldsymbol{\xi}_m^{\mathrm{T}} & \mathbf{d}_m^{\mathrm{T}}\end{bmatrix}^{\mathrm{T}} \tag{32}$$

Here, we use two inertia measurement units (IMU) (MPU9250) to measure the rotation between Frame 2 and Frame R, and four absolute encoders (US Digital MAE3) to measure the first four joints (θ_1 to θ_4). The WKMT kinematics and sensor setups are explained in detail in Appendix B.

C. Wrist Kinematics Regression via Sparsity Promoting EKF

Based on the aforementioned setups, the full WKI model is written in the EKF format as

$$\mathbf{x}_1 = \begin{bmatrix}\mathbf{p}^{\mathrm{T}} & \boldsymbol{\kappa}^{\mathrm{T}} & \boldsymbol{\kappa}_I^{\mathrm{T}}\end{bmatrix}^{\mathrm{T}}; \quad \mathbf{y}_1 = \mathbf{0}; \tag{33a}$$

$$\mathbf{f}_1(\mathbf{x}_1, \mathbf{u}_1, \mathbf{v}_1) = \begin{bmatrix}\mathbf{p} \\ \mathbf{g}_\kappa(\boldsymbol{\xi}_0, \boldsymbol{\xi}_m + \mathbf{v}_{1,\xi}) \\ \boldsymbol{\kappa}_I + c_I\mathbf{g}_\kappa(\boldsymbol{\xi}_0, \boldsymbol{\xi}_m + \mathbf{v}_{1,\xi})\end{bmatrix} + \mathbf{v}_{1,p} \tag{33b}$$

$$\mathbf{h}_{1,1}(\mathbf{x}_1, \mathbf{u}_1, \mathbf{w}_1) = \begin{bmatrix}r_w & \mathbf{d}_w - \mathbf{d}_m - \mathbf{w}_{1,d}\end{bmatrix}^{\mathrm{T}} \tag{33c}$$

$$\mathbf{h}_{1,2}(\mathbf{x}_1) = \begin{bmatrix}\|\boldsymbol{\xi}_0\| - 1 & \boldsymbol{\kappa}_I^{\mathrm{T}}\end{bmatrix}^{\mathrm{T}} \tag{33d}$$

$$\mathbf{h}_{1,a}(\mathbf{x}_1, \mathbf{u}_1, \mathbf{w}_1) = \begin{bmatrix}\mathbf{h}_{1,1}^{\mathrm{T}}(\mathbf{x}_1, \mathbf{u}_1, \mathbf{w}_1) & \mathbf{h}_{1,2}^{\mathrm{T}}(\mathbf{x}_1)\end{bmatrix}^{\mathrm{T}} \tag{33e}$$

$$\mathbf{h}_1(\mathbf{x}_1, \mathbf{u}_1, \mathbf{w}_1) = \begin{bmatrix}\mathbf{h}_{1,a}(\mathbf{x}_1, \mathbf{u}_1, \mathbf{w}_1) + \mathbf{w}_{1,h} \\ \gamma(\mathbf{p}_s) + \mathbf{w}_{1,\gamma}\end{bmatrix} \tag{33f}$$

where $\mathbf{p}_s = [\mathbf{c}_f,\ \mathrm{vec}^{\mathrm{T}}(\mathbf{D}_l),\ \mathrm{vec}^{\mathrm{T}}(\mathbf{D}_f)]^{\mathrm{T}}$; $\mathbf{g}_\kappa(\boldsymbol{\xi}_0, \boldsymbol{\xi}_m)$ is a function that calculates $\boldsymbol{\kappa}$ from $\boldsymbol{\xi}_0$ and $\boldsymbol{\xi}_m$ based on Eq. (18); $\mathbf{v}_1 = [\mathbf{v}_{1,\xi}^{\mathrm{T}},\ \mathbf{v}_{1,p}^{\mathrm{T}}]^{\mathrm{T}}$ and $\mathbf{w}_1 = [\mathbf{w}_{1,d}^{\mathrm{T}},\ \mathbf{w}_{1,h}^{\mathrm{T}},\ \mathbf{w}_{1,\gamma}^{\mathrm{T}}]^{\mathrm{T}}$ are respectively the process and measurement noise. Notice that $\mathbf{f}_1$ implies that the kinematic parameters are expected to be time-invariant. The observation function $\mathbf{h}_{1,1}$ is collected from Eqs. (22, 23). The additional observation function $\mathbf{h}_{1,2}$ provides better algorithm stability by ensuring that $\boldsymbol{\xi}_0$ is a unit quaternion, and the means of $\boldsymbol{\kappa}$ are centered around zeros through the discrete time integral of $\boldsymbol{\kappa}$ defined as $\boldsymbol{\kappa}_I \in \mathbb{R}^3$. The integral step $c_I > 0$ can be selected as $1/c_s$. $\mathbf{h}_{1,2}$ is designed to increase the robustness of regression without significantly affecting parameter identification governed by $\mathbf{h}_{1,1}$.

The state covariance $\mathbf{Q}_1$ and measurement covariance $\mathbf{R}_1$ for this model are designed as

$$\mathbf{Q}_1 = \begin{bmatrix} \mathbf{Q}_{1,\xi} & \mathbf{0} \\ \mathbf{0} & \mathbf{Q}_{1,p} \end{bmatrix}; \quad \mathbf{R}_1 = \begin{bmatrix} \mathbf{R}_{1,d} & \mathbf{0} & \mathbf{0} \\ \mathbf{0} & \mathbf{R}_{1,h} & \mathbf{0} \\ \mathbf{0} & \mathbf{0} & \mathbf{R}_{1,\gamma} \end{bmatrix} \tag{34}$$

where $\mathbf{Q}_{1,\xi}$ and $\mathbf{Q}_{1,p}$ are respectively corresponding to $\mathbf{v}_{1,\xi}$ and $\mathbf{v}_{1,p}$; $\mathbf{R}_{1,d}$, $\mathbf{R}_{1,h}$ and $\mathbf{R}_{1,\gamma}$ are respectively corresponding to $\mathbf{w}_{1,d}$, $\mathbf{w}_{1,h}$, and $\mathbf{w}_{1,\gamma}$. Specifically, $\mathbf{R}_{1,\gamma}$ is a diagonal matrix. This leads to the cost function

$$\begin{aligned} \mathcal{J}_1(\bar{\mathbf{x}}_{1,k}) = \big(&\mathbf{h}_{1,a}^{\mathrm{T}}(\bar{\mathbf{x}}_{1,k}, \mathbf{u}_{1,k}, \mathbf{0})(\mathbf{H}_{w,1,d,k}\mathbf{R}_{1,d}\mathbf{H}_{w,1,d,k}^{\mathrm{T}} \\ &+ \mathbf{R}_{1,h})^{-1}\mathbf{h}_{1,a}(\bar{\mathbf{x}}_{1,k}, \mathbf{u}_{1,k}, \mathbf{0})\big) \\ &+ (\bar{\mathbf{x}}_{1,k} - \hat{\mathbf{x}}_{1,k})^{\mathrm{T}}\hat{\mathbf{P}}_{xx,1,k}^{-1}(\bar{\mathbf{x}}_{1,k} - \hat{\mathbf{x}}_{1,k}) \\ &+ \boldsymbol{\gamma}^{\mathrm{T}}(\bar{\mathbf{p}}_{s,k})\mathbf{R}_{1,\gamma}^{-1}\boldsymbol{\gamma}(\bar{\mathbf{p}}_{s,k}) \end{aligned} \tag{35}$$

where $\mathbf{H}_{w,1,d,k} = \partial \mathbf{h}_{1,a}(\bar{\mathbf{x}}_{1,k}, \mathbf{u}_{1,k}, \mathbf{w}_{1,k})/\partial \mathbf{w}_{1,d,k}$.

The function $\boldsymbol{\gamma}(\mathbf{x})$ in Eq. (33, 35) is designed for increasing the sparsity of the parameters. When correctly designed and implemented, sparse model regression can identify the basis of a signal with the redundant states converging to zero. Sparsity can be promoted by ℓ-1 minimization [29], [30]. For Eq. (35), this requires $\boldsymbol{\gamma}(\mathbf{x}) = |\mathbf{x} - \mathbf{x}_b|^{0.5}$ where $\mathbf{x}_b$ is the user-defined bias introduced because some internal states (e.g., unit quaternions) are unable to reach zeros due to constraints.

Traditional ℓ-1 minimization via Kalman filtering may also require reconstructing the model [29] due to $|\mathbf{x} - \mathbf{x}_b|$ being undifferentiable at $\mathbf{x} = \mathbf{x}_b$. In this study, we use an alternative $\boldsymbol{\gamma}(\mathbf{x})$, which is a non-negative scalar function designed as

$$\gamma(\mathbf{x}) = \left(\sum \left(\boldsymbol{\alpha}^2 * (\mathbf{x} - \mathbf{x}_b)^2 + \boldsymbol{\sigma}^2\right)^{0.5} - \boldsymbol{\sigma}\right) + \sigma_0\right)^{0.5} - \sigma_0^{0.5} \tag{36}$$

whose partial derivative of $\mathbf{x}$ is

$$\frac{\partial \gamma}{\partial \mathbf{x}} = \frac{(\boldsymbol{\alpha}^2 * (\mathbf{x} - \mathbf{x}_b) * (\boldsymbol{\alpha}^2 * (\mathbf{x} - \mathbf{x}_b)^2 + \boldsymbol{\sigma}^2)^{-0.5})^{\mathrm{T}}}{2(\gamma + \sigma_0^{0.5})} \tag{37}$$

Here, $\boldsymbol{\alpha} > 0$ is a constant scaling parameter vector; $\boldsymbol{\sigma}$ and σ_0 are small positive constant parameters. Notice that when $x = 0$, Eqs. (36) and (37) both reach zeros; when $\boldsymbol{\sigma} \ll |\boldsymbol{\alpha} * (\mathbf{x} - \mathbf{x}_b)|$, $\boldsymbol{\gamma}^2(\mathbf{x}, \boldsymbol{\alpha}, \boldsymbol{\sigma})$ is approximately identical to the sum of $|\boldsymbol{\alpha} * (\mathbf{x} - \mathbf{x}_b)|$. Therefore, $\boldsymbol{\alpha}$ is selected to scale $(\mathbf{x} - \mathbf{x}_b)$ to proper magnitudes for optimization; $\boldsymbol{\sigma}$ and σ_0 are designed as reasonably small numbers compared to $|\boldsymbol{\alpha} * (\mathbf{x} - \mathbf{x}_b)|$. The user can also design $\mathbf{R}_{1,\gamma}$ to adjust the weight of the sparsity promoting term in the cost function. Since Eq. (36) is a smooth function, it can directly fit into the EKF structure.

In summary, the real-time WKI algorithm is designed based on a sparsity-promoting EKF (SP-EKF), which is expected to reduce the model complexity by prioritizing the primary wrist parameters, and drives the sparse parameters $\mathbf{p}_s$ to zeros. SP-EKF can also potentially improve the robustness of the regression algorithm under noisy conditions. The next section verifies the findings in Section II and III through simulation.

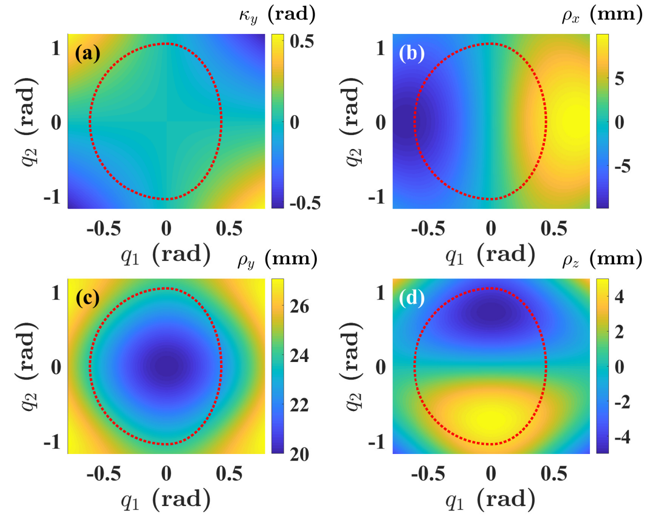

Fig. 5. The solutions of the constrained rotation κ_y and translational displacement $\boldsymbol{\rho}_0$ from the ellipsoidal joint model in the domain of $\mathbf{q}$, where (a) shows the solution of κ_y; (b) shows the solution of ρ_x; (c) presents the solution of ρ_y; and (d) presents the solution of ρ_z. The range of q_1 and q_2 in these plots are respectively $[-\pi/4,\ \pi/4]$ and $[-3\pi/8,\ 3\pi/8]$. The red dot contour is the approximate wrist circumduction envelope [6].

IV. Numerical Simulation

This section presents the numerical simulations to demonstrate the theoretical findings and test the performance of the WKI algorithm. The simulations are carried out in MATLAB. The default forearm and wrist parameters are selected as [37]

$$c_{\rho,1} = 3 \text{ cm}; \quad c_{\rho,2} = 2 \text{ cm}; \quad c_{\rho,3} = 2.5 \text{ cm} \tag{38a}$$

$$\mathbf{d}_0 = \begin{bmatrix} 1 & 12 & -1 \end{bmatrix}^{\mathrm{T}} \text{ cm}; \quad \mathbf{d}_1 = \begin{bmatrix} -2 & 10 & 1 \end{bmatrix}^{\mathrm{T}} \text{ cm} \tag{38b}$$

A. Solutions of the Ellipsoidal Joint Model

The solutions of the constrained rotation κ_y and translational displacement $\boldsymbol{\rho}_0$ respectively from Eq. (4) and Eq. (A-2) in the domain of $\mathbf{q}$ are presented in Fig. 5. Notice that all of these maps are symmetric and bounded within the domain of $\mathbf{q}$, where ρ_x and ρ_z are respectively sensitive to κ_z and κ_x (i.e., q_1 and q_2), and ρ_y can increase along any rotation directions due to the sliding of ellipsoid ball in the socket as previously depicted in Fig. 3. Figure 5(a) also shows that the rotation constrained by Eq. (2) is non-orthogonal, as the coupling between RUD and FE becomes significant when both q_1 and q_2 are large.

The wrist kinematics in real life is more complicated than the proposed ellipsoidal joint. In the upcoming WKI simulations, a few references are employed to test the generality of the proposed approach based on Eqs. (22, 23) in regressing different models and uncertainties. To begin with, three translational displacement references $\mathbf{d}_{r,i}$ $(i = 1, 2, 3)$ are adopted as

$$\mathbf{d}_{r,i}(\boldsymbol{\kappa}) = \mathbf{d}_0 + \boldsymbol{\Omega}_0\boldsymbol{\Omega}_\kappa\mathbf{d}_1 + \boldsymbol{\Omega}_0\boldsymbol{\rho}_i \tag{39a}$$

$$\boldsymbol{\rho}_1 = \mathbf{0}; \quad \boldsymbol{\rho}_2 = \boldsymbol{\Omega}_\psi\mathbf{d}_{0,1}; \quad \boldsymbol{\rho}_3 = \boldsymbol{\rho}_0 + \mathbf{D}_l\mathbf{q} \tag{39b}$$

so that $\mathbf{d}_{r,1}$ is the simplified reference that excludes wrist translation $\boldsymbol{\rho}$; $\mathbf{d}_{r,2}$ is similar as in [34], [35], where a constant

This article has been accepted for publication in a future issue of this journal, but has not been fully edited. Content may change prior to final publication. Citation information: DOI 10.1109/TBME.2021.3111878, IEEE Transactions on Biomedical Engineering

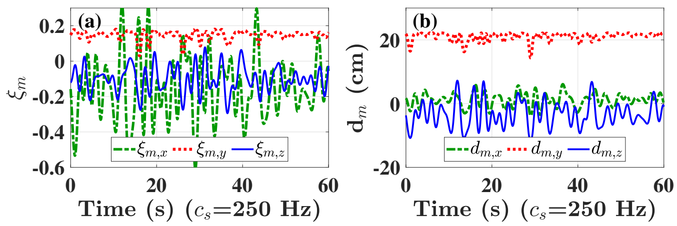

Fig. 6. The quasi-periodic wrist motions trajectories randomly generated by the simulation reference model, where (a) shows the x, y, and z components of wrist rotation quaternion $\boldsymbol{\xi}_m$ (note that $\|\boldsymbol{\xi}_m\| = 1$), and (b) shows the wrist translation displacement $\mathbf{d}_m$ (where $\mathbf{d}_m = \mathbf{d}_{r,1}$ based on Eq. (39)).

offset divides FE-RUD-FE-RUD joint into two halves (recall $\boldsymbol{\Omega}_{\kappa,3} = \boldsymbol{\Omega}_\psi \boldsymbol{\Omega}_\psi$); and $\mathbf{d}_{r,3}$ features the proposed ellipsoid-based translation in Eq. (A-1) along with a $\mathbf{q}$-affine term.

We also respectively adopt three rotation references as the sequential rotation models $\boldsymbol{\Omega}_{\kappa,1}$ (first-RUD-then-FE), $\boldsymbol{\Omega}_{\kappa,2}$ (first-FE-then-RUD), and $\boldsymbol{\Omega}_{\kappa,3}$ (RUD-FE-RUD-FE) from Eqs. (5, 8, 11) for different case studies. The default value of the quaternion $\boldsymbol{\xi}_0$ that represents $\boldsymbol{\Omega}_0$ is selected as

$$\boldsymbol{\xi}_0 = \begin{bmatrix} 0.9710 & -0.1539 & 0.1499 & -0.1050 \end{bmatrix}^{\mathrm{T}} \tag{40}$$

which is equivalent to the z-y-x Euler angle $\boldsymbol{\kappa}_0 = [-20°, 15°, -15°]^{\mathrm{T}}$. Hence, these reference models generate the trajectories of input $\mathbf{u}_1$ in Eq. (32), which are used as regression data in the following WKI simulations.

B. Parameter Identification via EKF

We use the first simulation to show that EKF is a real-time optimizer, where translational reference is $\mathbf{d}_{r,1}$, and the regression model from Eqs. (22, 23) is simplified to exclude $\mathbf{q}$-affine and FLC terms. Figure 6 shows an example wrist trajectories of $\boldsymbol{\xi}_m$ and $\mathbf{d}_m$ generated by the reference model via quasi-periodic trajectories of $\mathbf{q}$, which are composed by harmonic waves of random amplitudes and phases. The trajectories are sampled at 250 Hz with zero noise added.

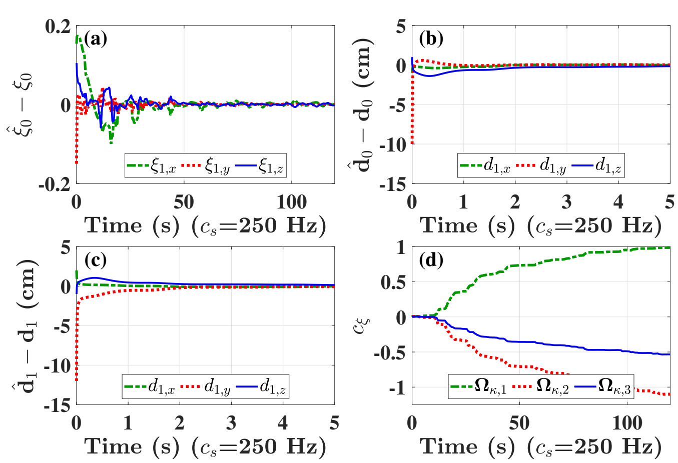

Fig. 7. Trajectories of parameter estimation errors in the regression of the simplified model via EKF, where (a) shows the estimation error of $\boldsymbol{\xi}_0$; (b) shows the estimation error of $\mathbf{d}_0$; (c) shows the estimation error of $\mathbf{d}_1$; and (d) shows the estimation of c_ξ under different sequential rotation models $\boldsymbol{\Omega}_{\kappa,1}$, $\boldsymbol{\Omega}_{\kappa,2}$, and $\boldsymbol{\Omega}_{\kappa,3}$ from Eqs. (5, 8, 11).

To test if EKF can correct large initial guess errors, the WKI simulation starts with initial estimations as zeros, except that $\boldsymbol{\xi}_0 = [1,\ 0,\ 0,\ 0]^{\mathrm{T}}$. The covariance matrices are selected as

$$\mathbf{P}_{xx,0} = 10^{-6}\mathbf{I}_{14};\quad \mathbf{Q}_{1,u} = 10^{-6}\mathbf{I}_4 \tag{41a}$$

$$\mathbf{Q}_{1,p} = \mathrm{diag}(\begin{bmatrix} 10^{-8}\mathbf{1}_5^{\mathrm{T}} & 10^{-10}\mathbf{1}_{12}^{\mathrm{T}} \end{bmatrix}) \tag{41b}$$

$$\mathbf{R}_{1,u} = 10^{-6}\mathbf{I}_3;\quad \mathbf{R}_{1,h} = \mathrm{diag}(\begin{bmatrix} 10^{-6}\mathbf{1}_5^{\mathrm{T}} & \mathbf{1}_3^{\mathrm{T}} \end{bmatrix}) \tag{41c}$$

The results are shown in Fig. 7. Figures 7(a-c) is based on the reference model whose rotation is governed by $\boldsymbol{\Omega}_{\kappa,1}$. The estimated parameters $\hat{\boldsymbol{\xi}}_0$, $\hat{\mathbf{d}}_0$, and $\hat{\mathbf{d}}_1$ eventually converge to the close vicinities of their true values. Also, the convergence of translational parameters $\hat{\mathbf{d}}_0$ and $\hat{\mathbf{d}}_1$ is significantly faster than that of the quaternion parameters $\hat{\boldsymbol{\xi}}_0$. This is likely due to the observation errors being less sensitive to $\hat{\boldsymbol{\xi}}_0$. Finally, Fig. 7(d) compares the values of c_ξ in Eq. (23) from the rotation constraint regressions based on different rotation references. The values of c_ξ converge to approximately 1, -1, and -0.5 with respect to $\boldsymbol{\Omega}_{\kappa,1}$, $\boldsymbol{\Omega}_{\kappa,2}$, and $\boldsymbol{\Omega}_{\kappa,3}$, which corroborates the findings in Section II-C revealing that c_ξ can approximate and classify different rotation models.

C. Characteristics of FLC and SP-EKF

The previous subsection confirms that EKF is capable of real-time parameter identification. For the simulations involving SP-EKF, we use the full regression model in Eqs. (22, 23), which contains 119 unknown kinematic parameters. The covariances are selected as

$$\mathbf{P}_{xx,0} = 10^{-6}\mathbf{I}_{119};\ \mathbf{Q}_{1,p} = \mathrm{diag}(\begin{bmatrix} 10^{-8}\mathbf{1}_5^{\mathrm{T}}\ 10^{-10}\mathbf{1}_{114}^{\mathrm{T}} \end{bmatrix}) \tag{42}$$

The regression model updated by regular EKF can obtain good approximation of wrist kinematics. However, the FLC in the regression model can lead to redundancy, which leads to poor identification of primary parameters $\hat{\boldsymbol{\xi}}_0$, c_ξ, $\hat{\mathbf{d}}_0$, and $\hat{\mathbf{d}}_1$. Hence, the covariances and parameters introduced by SP-EKF are

$$\mathbf{R}_{1,\lambda} = 1;\ \boldsymbol{\alpha} = 10;\ \mathbf{x}_b = 0;\ \boldsymbol{\sigma} = 10^{-5};\ \sigma_0 = 10^{-5} \tag{43}$$

The proposed WKI approach is tested on two reference models. The first reference model adopts $\mathbf{d}_{r,2}$ as translation and $\boldsymbol{\Omega}_{\kappa,3}$ as rotation [34], [35], where $\mathbf{d}_{0,1} = [0.120]$ cm; and the second reference model adopts $\mathbf{d}_{r,3}$ as translation and $\boldsymbol{\Omega}_{\kappa,2}$ as rotation, where $\mathbf{D}_l = [0,\ 0;\ 0,\ -2;\ 0,\ 0]$ cm. For each case, the SP-EKF updates the regression models for 3×10^4 steps within 2 minutes. The norms of translational displacement estimation error $\|\mathbf{d}_w - \mathbf{d}_m\|$ and rotational constraint estimation error $|r_w|$ from the updated models are then mapped in the domain of κ_z and κ_x (i.e., q_1 and q_2). As shown in Fig. 8, for translational regressions, the envelopes of wrist circumduction movements [6] are contained within the regions of $\|\mathbf{d}_w - \mathbf{d}_m\| \leq 1.5$ mm for the first reference ($\mathbf{d}_m = \mathbf{d}_{r,2}$), and $\|\mathbf{d}_w - \mathbf{d}_m\| \leq 3$ mm for the second reference ($\mathbf{d}_m = \mathbf{d}_{r,3}$). These estimation errors are respectively within 1% and 2% of the ranges of $\|\mathbf{d}_m\|$, which are approximately 15 cm for both cases. The results also indicate that the proposed ellipsoid-based translation $\boldsymbol{\rho}_0$ in Eq. (A-1) is relatively more complicated and difficult to model. For rotational regressions, the circumduction envelopes are largely contained within the

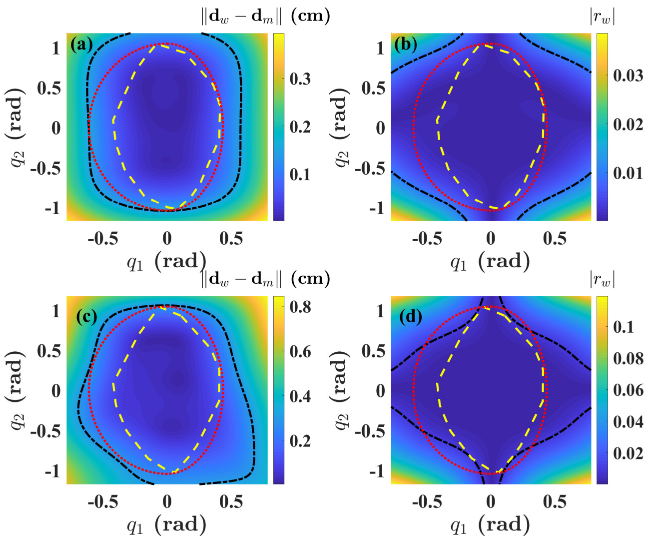

Fig. 8. The performance of WKI algorithm on regressing two reference models, where (a, c) and (b, d) map the norms of estimation errors in translational displacement $\|\mathbf{d}_w - \mathbf{d}_m\|$ and rotational constraint $|r_w|$, respectively. Here, (a, b) are results from the first reference (with $\mathbf{d}_{r,2}$ and $\mathbf{\Omega}_{\kappa,3}$); (c, d) are results from the second reference (with $\mathbf{d}_{r,3}$ and $\mathbf{\Omega}_{\kappa,2}$). In the maps, the yellow dash countour contains the region traversed by the motion trajectory $\mathbf{q}$; the red dot contour is the circumduction envelope of the wrist motions [6]. The black dot-dash contours in (a) and (c) contains the regions where $\|\mathbf{d}_w - \mathbf{d}_m\| \leq 1.5$ mm and $\|\mathbf{d}_w - \mathbf{d}_m\| \leq 3$ mm, respectively; and the black dot-dash contours in (b, d) contains the regions where $|r_w| < 0.01$.

regions of $|r_w| \leq 0.01$ for both cases, which are within 5% of the range of quaternion-based constraint $|r_\kappa|$ as calculated from Eq. (3). Hence, the WKI algorithm is general and can approximate various reference models. The second reference (with $\mathbf{d}_{r,3}$ and $\mathbf{\Omega}_{\kappa,2}$) is also used in the later simulations.

We then compares three different regression configurations: the simplified regression model (with no FLC) updated by regular EKF, the full model updated by regular EKF, and the full

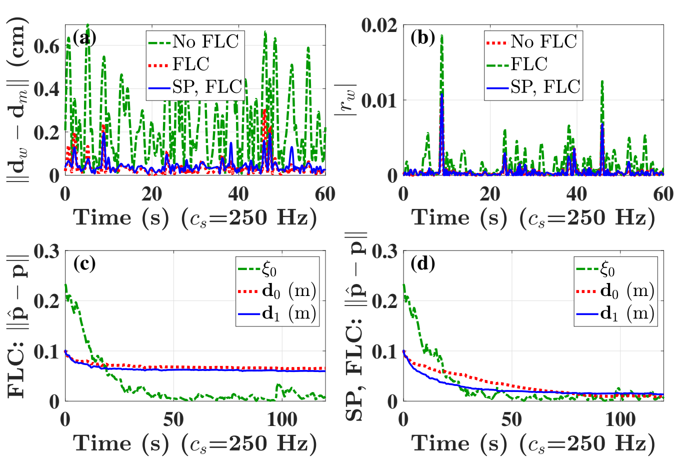

Fig. 9. The comparison of regression performances using a simplified regression model (no FLC), a full model updated by regular EKF, and a full model updated by SP-EKF, where (a) compares the norm of the translational displacement estimation error $\|\mathbf{d}_w - \mathbf{d}_m\|$; (b) compares the norm of estimated rotation constraint $|r_w|$ (whose true value is zero); (c) and (d) demonstrates the norm of the primary parameter estimation errors from the regression model with FLC respectively updated by regular EKF and SP-EKF.

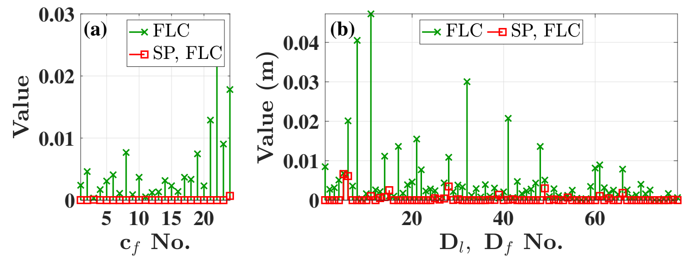

Fig. 10. The comparison of parameter sparsities (zeros versus non-zeros) of the models respectively updated by regular EKF and SP-EKF, where (a) shows the rotational parameter values from $\mathbf{c}_f$, and (b) presents the translational parameter values from $\mathbf{D}_l$ and $\mathbf{D}_f$.

model updated by SP-EKF. From Fig. 9(a), we observe that the full regression model excels in translational displacement estimations. This confirms that FLC is effective in modeling the nonlinear kinematics introduced by $\boldsymbol{\rho}_0$ from the reference $\mathbf{d}_{r,3}$. For quaternion-based constraint regression shown in Fig. 9(b), the benefit from FLC is not significant, since the reference rotation $\mathbf{\Omega}_{\kappa,2}$ can be closely approximated with the term $c_\xi \sin(\kappa_x/2)\sin(\kappa_z/2)$ from Eq. (23). While models updated by regular EKF can achieve good approximation, regular EKF cannot prioritize the identification of primary parameters $\boldsymbol{\xi}_0$, c_ξ, $\mathbf{d}_0$, and $\mathbf{d}_1$ as shown in Fig. 9(c). SP-EKF, on the other hand, ensures the convergence of these parameters to the vicinity of their true values as shown in Fig. 9(d). Figure 10 indicates that SP-EKF also significantly decreases the number of the nonzero parameters, leading to simpler models suitable for further analysis.

SP-EKF also provides robustness towards noises. To demonstrate this, the translational and rotational motion data are overlaid with high-frequency quasi-period noises, whose ranges are ± 2 mm and $\pm 2°$, respectively. In Figs. 11(a, b), we observe that SP-EKF yields better regressions under noises, particularly in translational displacement estimations. Figures 11(c, d) show that SP-EKF can also identify primary kinematic parameters despite the noises.

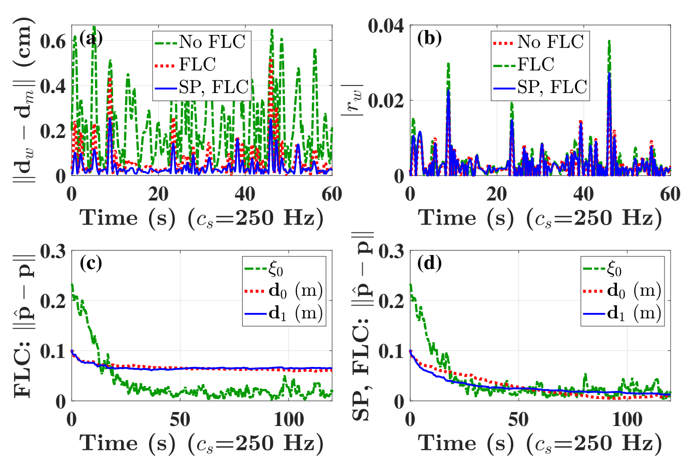

Fig. 11. The comparison of regression performances using a simplified regression model (no FLC), a full model updated by regular EKF, and a full model updated by SP-EKF based on noisy motion data. The specifications of the subplots are the same as those in Fig. 9.

This article has been accepted for publication in a future issue of this journal, but has not been fully edited. Content may change prior to final publication. Citation information: DOI 10.1109/TBME.2021.3111878, IEEE Transactions on Biomedical Engineering

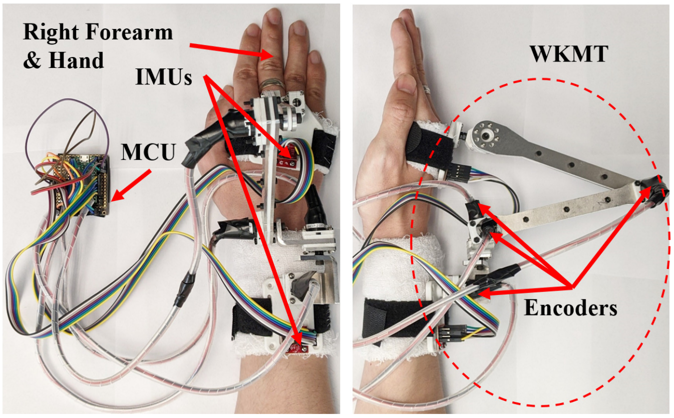

Fig. 12. The experimental setup: the author wears the WKMT via sleeves/bands and Velcro tapes on his right forearm. The IMU sensors are installed on the base parts attached to the forearm and hand dorsum. The encoder locations on the WKMT are also marked. The sensor data is collected by a microchip processor (MCU), which transmits the data to a computer.

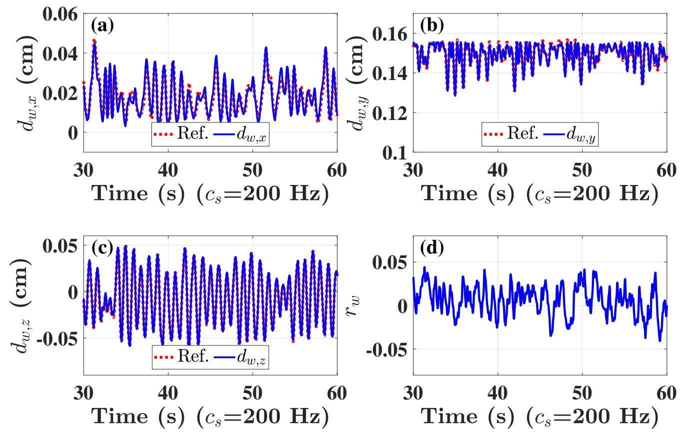

Fig. 14. The estimation performance of a model with FLC terms updated by SP-EKF based on 30 seconds of experimental motion data (sampling rate $c_s = 200$). The x, y, and z components of $\mathbf{d}_w$ and their references from $\mathbf{d}_m$ are shown respectively in (a, b, c); the trajectory of r_w is shown in (d).

The simulations show that the proposed regression model in Eqs. (22, 23) can approximate various reference models. The potentials of SP-EKF in reducing model complexity, prioritizing identification of primary parameters, and providing robustness towards noises are also observed. In the next section, experiments are carried out with WKMT to further validate the proposed WKI approach.

V. Experimental Validation

Experimental validation of the proposed WKI algorithm is carried out based on wrist motion data collected by WKMT. The experimental setup is shown in Fig. 12. The wearability of WKMT is similar to that of TAWE exoskeleton discussed in Section I. WKMT is attached to the human body through Velcro tapes, which indicates that wearing locations can slowly shift over time. Therefore, the wrist kinematic parameter $\mathbf{q}$ from Eq. (24) is assumed to be slowly time-varying.

The user is asked to keep randomly moving the wrist during data collections. The WKMT samples wrist motions at a rate of 200 Hz. The measurement noises are eliminated by a 10-Hz low-pass filter. Note that the filter should be carefully selected to avoid distortion of real wrist movements. An example of the processed rotation trajectory of $\boldsymbol{\xi}_m$ is shown in Fig. 13(a). The translational displacement $\mathbf{d}_m$ of the wrist in the 3D space is shown in Fig. 13(b, c) from different viewing aspects. It is observed that the distribution of the translational displacements are approximately located on a surface, which indicates that it is valid to model the wrist as a 2-DOF joint.

To compare different regression setups, the data are regressed offline. However, the proposed WKI algorithm is efficient for real-time application, and can run at 1100 Hz on a 3.6 GHz Processor (AMD Ryzen 7 1800X). The configurations of EKF and initial estimations are the same as in Section IV, except that the covariance matrix $\mathbf{Q}_{1,p}$ has been updated to $\mathbf{Q}_{1,p} = 10^{-10}\mathbf{I}_{119}$ for more steady estimations of $\boldsymbol{\xi}_0$ and c_ξ.

A. Regression Performance

The wrist kinematics estimation performance of a model with FLC updated by SP-EKFs is presented in Fig. 14. After 6000 steps of update within 30 seconds, the model closely approximates the translational displacements. The norm of maximum translational estimation error is around 5 mm, which

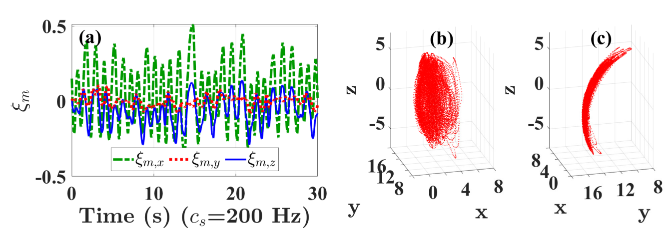

Fig. 13. The experimental wrist motion data, where (a) shows the x, y, and z components of $\boldsymbol{\xi}_m$, and (b, c) presents the translational displacement in a 3D space from different view angles. The axis units in (b, c) are centimeters.

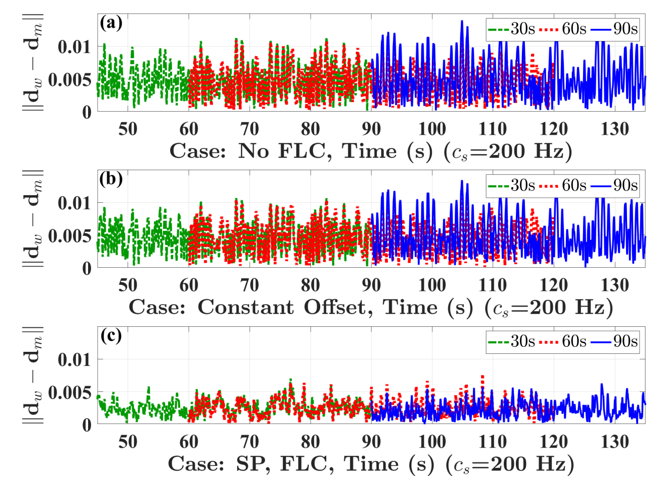

Fig. 15. The norms of translational displacement estimation errors $\|\mathbf{d}_w - \mathbf{d}_m\|$ from different WKI setups based on experimental data, where (a) uses a simplified model without FLC; (b) adopts a model with a model with a constant offset amid the rotation (i.e., $\mathbf{d}_{r,2}$); and (c) uses the proposed model updated with SP-EKF. For each case, three 60-second tests are carried out, which are respectively based on models updated for 30, 60, and 90 seconds.

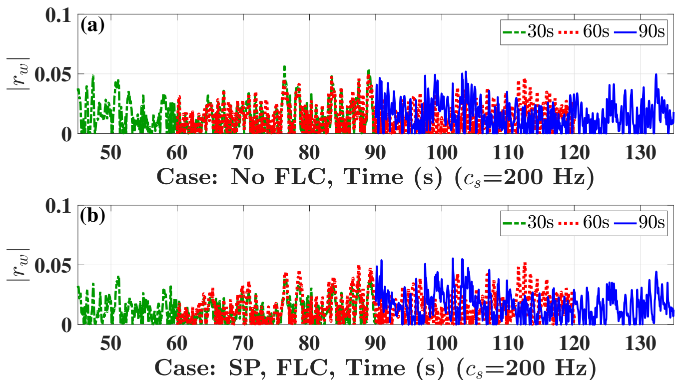

Fig. 16. The norm of rotational constraint estimation errors $|r_w|$ (whose truth is zero) from different WKI setups based on experimental data, where (a) uses a simplified model without FLC; (b) uses the proposed model updated with SP-EKF. For each case, three 60-second tests are carried out, which are respectively based on models updated for 30, 60, and 90 seconds.

is below 5% of the total range of wrist translational displacement. The absolute value of quaternion-based constraint regression is contained within 0.05.

The consistency of real-time regressions as well as the comparison of different WKI configurations are shown in Figs. 15 and 16. For each configurations, three 60-second estimation tests are carried out, which are respectively based on models updated for 30, 60, and 90 seconds (6000 updates between one model and another). For translational regressions, we respectively adopt a simplified model without FLC, a model with a constant offset amid the rotation (i.e., $\mathbf{d}_{r,2}$ from Eq. (39)), and the proposed model updated with SP-EKF. The first two cases yield similar performances as shown Figs. 15(a, b), and the proposed model excels in regression accuracy with 50% smaller estimation errors as shown in Fig. 15(c).

The rotational constraint estimation errors are compared in Fig. 16. Similar to the simulations, FLC does not significantly improve the regression performance. In general, we

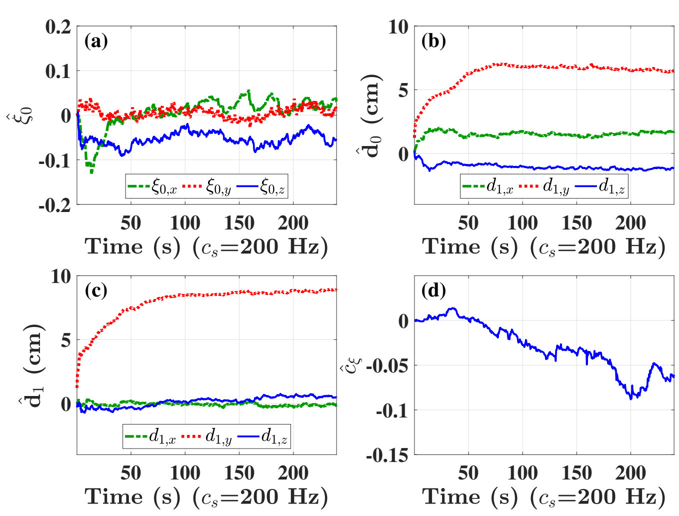

Fig. 17. The estimated primary parameters from the model with FLC trained by SP-EKF, where (a) shows the estimation of the x, y, and z components of $\boldsymbol{\xi}_0$, (b) presents the estimation $\hat{\mathbf{d}}_0$, and (c) shows the estimation $\hat{\mathbf{d}}_1$, and (d) presents the identification of $\hat{c}_\xi$.

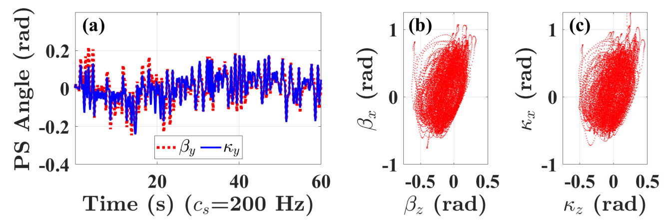

Fig. 18. The comparison between wrist rotation presented in Frame R and Frame 0. Here, (a) shows the angle β_y and κ_y on pronation-supnation direction, (b) shows the RUD-FE trajectory in Frame R, (c) shows the RUD-FE trajectory in Frame 0. (Note - $+z$: radial deviation, $-z$: ulnar deviation, $+x$ extension, $-x$: flexion).

also observe larger rotational constraint estimation errors from experiments than from simulations. Apart from slowly varying wrist kinematics, the observation also suggests that the real wrist rotation may be much more complicated.

Figures 15 and 16 also show the real-time adaptability of the WKI algorithm. In the overlapped estimation windows of two models, the model updated with the newer data yields different and potentially smaller estimation errors. This also indicates that the proposed real-time WKI algorithm can keep up with slowly varying kinematic properties.

B. Analysis of the Identified Model

Since the wrist motion data is filtered before regression, the experiments do not distinctively show the robustness of SP-EKF towards noise. However, SP-EKF ensures the identifications of the primary wrist kinematic parameters as shown in Fig. 17. The displacements $\hat{\mathbf{d}}_0$ and $\hat{\mathbf{d}}_1$ are reasonable according to the user forearm profile, especially on the y (distal) direction. The identified $\hat{c}_\xi$ is close to zero, which suggests no similarity to any sequential rotations (e.g., first-RUD-then-FE rotation $\boldsymbol{\Omega}_{\kappa,1}$, first-FE-then-RUD rotation $\boldsymbol{\Omega}_{\kappa,2}$).

The effect of the identified $\hat{\boldsymbol{\xi}}_0$ is demonstrated in Fig. 18. Here, $\boldsymbol{\beta}$ is the z-y-x Euler angle corresponding to $\boldsymbol{\xi}_m$. Recall from Fig.2 that β is the rotation of Frame 2 in Frame R, and κ is the rotation of Frame 2 in Frame 0. As shown in Fig. 18(a), on the pronation-supination (PS) direction, the angle κ_y measured in Frame 0 is slightly smaller than β_y measured in Frame R. The FE-RUD trajectories in Frame R and Frame 0 are respectively presented in Fig. 18(b, c). Notice that the oblique ellipsoidal shape of the RUD-FE trajectory is also previously witnessed in other studies [7], [38], [39]. As the observation function $\mathbf{h}_{1,2}$ from Eq. (33) drives the mean values of κ to zeros by converging the integral term κ_I, the RUD-FE trajectory in Fig. 18(c) is shifted to center around the origin. Note that this does not deny the correctness of Fig. 18(b), since Figs. 18(b) and (c) respectively display the same wrist rotation in two different frames.

C. Remarks and Limitations

In general, the experimental results corroborate the simulation observations. The proposed WKI algorithm is proved capable of identifying wrist kinematics in real-time. The regression model with FLC updated by SP-EKF can approximate

This article has been accepted for publication in a future issue of this journal, but has not been fully edited. Content may change prior to final publication. Citation information: DOI 10.1109/TBME.2021.3111878, IEEE Transactions on Biomedical Engineering

the wrist motion with good accuracy, and provide useful wrist kinematic information for analysis.

However, wearable devices such as WKMT can introduce soft tissue artefacts due to deformations of muscles and skins. These model uncertainties can cause measurement errors and affect modeling accuracy. Hence, the performance of the proposed WKI algorithm remains to be further validated based on alternate measurements with soft tissue artefact mitigation (e.g., stereophotogrammetry [40], [41]).

Finally, the experiment based on WKMT emulates the future use of the proposed method in TAWE. Wrist tremors are real human movements governed by the wrist biomechanics of the patient. Therefore, we hypothesize no significant difference when the proposed algorithm is applied to a tremor-affected user, which will be investigated in future studies.

VI. Conclusion and Future Work

This paper proposed a novel method for real-time wrist kinematics identification (WKI). We designed the regression model based on ellipsoidal joint formulation, which features a quaternion-based constraint that characterizes the constrained wrist rotation. The regression model also employs 2D Fourier linear combiners (FLC) to approximate unmodeled nonlinear wrist kinematic features. Extended Kalman filter (EKF) was implemented to update the model in real-time based on wrist motion data. A sparsity-promoting EKF (SP-EKF) was also realized through a smooth $\ell 1$-minimization observation function that utilizes the optimality of EKF. To test the WKI algorithm and compare different regression setups, simulations were carried out using various reference models. Observations from simulations showed that: (1) the proposed model with FLC can accurately approximate various reference models; (2) the quaternion-based constraint can regress and classify different sequential rotational models; and (3) SP-EKF can provide accurate regression with reduced model complexity, and robustness towards noise. We also developed a wrist kinematic measurement tool (WKMT) to collect wrist motion data for experimental validation. The experimental results corroborated the findings from simulations. The experiment also showed that the proposed real-time WKI algorithm can adapt to slowly time-varying properties, and identify primary wrist kinematic parameters that are useful for analysis. While motivated by the development of TAWE exoskeleton for wrist tremor suppression, the proposed method can be applied to generic wrist kinematics modeling problems. The framework of proposed method may also apply to the real-time identifications of other joints for exoskeleton control.

The experimental results showed that there is still room for improvement in the rotation model regression. In the future, we will explore more accurate wrist kinematic modeling through extensive experiments. We will also integrate the real-time WKI algorithm into the control framework of TAWE, and test its performance in wrist tremor suppression.

Appendix A
Explicit Solution of $\boldsymbol{\rho}_0$

The explicit solution of $\boldsymbol{\rho}_0$ in terms of $\boldsymbol{\kappa}$ and $\mathbf{c}_\rho$ is

$$\boldsymbol{\rho}_0 = \begin{bmatrix} a_1/a_4 & a_2 & a_3/a_4 \end{bmatrix}^{\mathrm{T}} \tag{A-1}$$

where

$$\begin{aligned} a_1 = &- \Big[c_{\rho,3}^2 \cos(\zeta_x)\big(\sin(\zeta_x)\sin(\zeta_y) - c_{\rho,1}^2 \sin(\zeta_x)\sin(\zeta_y) \\ &+ (c_{\rho,1}^2 - c_{\rho,2}^2)\sin(\zeta_x)\sin(\zeta_y)\cos^2(\zeta_z) \\ &+ (c_{\rho,2}^2 - c_{\rho,1}^2)\cos(\zeta_y)\sin(\zeta_z)\cos(\zeta_z)\big)\Big] \end{aligned} \tag{A-2a}$$

$$\begin{aligned} a_2 = &\big(c_{\rho,3}^2 \sin^2(\zeta_x) - c_{\rho,1}^2 \sin^2(\zeta_z)\sin^2(\zeta_x) + c_{\rho,1}^2 \sin^2(\zeta_z) \\ &+ c_{\rho,2}^2 \sin^2(\zeta_z)\sin^2(\zeta_x) - c_{\rho,2}^2 \sin^2(\zeta_z) \\ &- c_{\rho,2}^2 \sin^2(\zeta_x) + c_{\rho,2}^2\big)^{0.5} \end{aligned} \tag{A-2b}$$

$$\begin{aligned} a_3 = &- \Big[c_{\rho,3}^2 \cos(\zeta_x)\big(\cos(\zeta_y)\sin(\zeta_x) - c_{\rho,1}^2 \cos(\zeta_y)\sin(\zeta_x) \\ &+ (c_{\rho,1}^2 - c_{\rho,2}^2)\cos(\zeta_y)\sin(\zeta_x)\cos^2(\zeta_z) \\ &+ (c_{\rho,1}^2 - c_{\rho,2}^2)\sin(\zeta_z)\sin(\zeta_y)\cos(\zeta_z)\big)\Big] \end{aligned} \tag{A-2c}$$

$$\begin{aligned} a_4 = &\big(-c_{\rho,3}^2 \cos^2(\zeta_x) + c_{\rho,3}^2 - c_{\rho,1}^2 \cos^2(\zeta_z)\cos^2(\zeta_x) \\ &+ c_{\rho,1}^2 \cos^2(\zeta_x) + c_{\rho,2}^2 \cos^2(\zeta_z)\cos^2(\zeta_x)\big)^{0.5} \end{aligned} \tag{A-2d}$$

Here, $\boldsymbol{\zeta} = [\zeta_x,\ \zeta_y,\ \zeta_z]^{\mathrm{T}}$ is the y-x-z sequenced Euler angles that satisfies

$$\boldsymbol{\Omega}_\kappa(\boldsymbol{\kappa}) = \boldsymbol{\Omega}_y(\zeta_y)\boldsymbol{\Omega}_x(\zeta_x)\boldsymbol{\Omega}_z(\zeta_z) \tag{A-3}$$

Appendix B
Kinematics of WKMT

TABLE II
Properties of transformations between coordinate frames in the WKMT kinematic system.

From	To	Translation ($\mathbb{R}^3$)	Rotation ($\mathbb{R}^{3\times3}$)
R	J1	$\mathbf{d}_{\mathrm{R}} = [0;0;0]$ cm	$\boldsymbol{\Omega}_z(\theta_1)$
J1	J2	$\mathbf{d}_{\mathrm{J1}} = [1;4;3.5]$ cm	$\boldsymbol{\Omega}_y(\theta_2)$
J2	J3	$\mathbf{d}_{\mathrm{J2},x} = -0.3$ cm	$\boldsymbol{\Omega}_x(\theta_3)$
J3	J4	$\mathbf{d}_{\mathrm{J3},z} = 12$ cm	$\boldsymbol{\Omega}_x(\theta_4)$
J4	J5	$\mathbf{d}_{\mathrm{J4},y} = 12$ cm	$\boldsymbol{\Omega}_x(\theta_5)$
J5	J6	$\mathbf{d}_{\mathrm{J5},z} = -2$ cm	$\boldsymbol{\Omega}_z(\theta_6)$
J6	2	$\mathbf{d}_{\mathrm{J6}} = [0;0;0]$ cm	$\mathbf{I}_3$

As WKMT has 6 joints, a total of six intermediate (Frame J1-J6) are defined. The joint angles are defined as $\boldsymbol{\theta} = [\theta_1,\ \theta_2,\ \theta_3,\ \theta_4,\ \theta_5,\ \theta_6]$. For convenience, the origins of Frame R and Frame 2 are respectively defined to be on the interceptions between base parts and the axes of Joint 1 and Joint 6. The transformations between frames in the exoskeleton kinematic chain are demonstrated in Table II, where the default parameters of the design are also included. In the table, the terms marked as $d_{i,j}$ and $\boldsymbol{\Omega}_j$ stand for the translation and rotation along the j axis (in Frame i), respectively.

The rotation $\boldsymbol{\Omega}_m$ (or equivalently the rotation quaternion $\boldsymbol{\xi}_m$ in Eq.(17)) between Frame 2 and Frame R can be directly calculated with IMU measurements through sensor fusion [42]. Encoders are installed on the first four joints to measure θ_1, θ_2, θ_3, and θ_4. The unmeasured joint angles θ_5 and θ_6 can be calculated from the equation

$$\begin{aligned} \boldsymbol{\Omega}_{56} &= \big(\boldsymbol{\Omega}_z(\theta_1)\boldsymbol{\Omega}_y(\theta_2)\boldsymbol{\Omega}_x(\theta_3)\boldsymbol{\Omega}_x(\theta_4)\big)^{\mathrm{T}}\boldsymbol{\Omega}_m \\ &= \boldsymbol{\Omega}_x(\theta_5)\boldsymbol{\Omega}_z(\theta_6) \end{aligned} \tag{A-4}$$

which leads to

$$\theta_5 = \arctan\Big(-\frac{a_{56,2,3}}{a_{56,3,3}}\Big);\ \theta_6 = \arctan\Big(-\frac{a_{56,1,2}}{a_{56,1,1}}\Big) \tag{A-5}$$

where $a_{56,i,j}$ is the ith row, jth column element of $\mathbf{\Omega}_{56}$. Hence, with the full knowledge of $\boldsymbol{\theta}$, we can calculate the translational displacement $\mathbf{d}_m$ between Frame 2 and Frame R based on kinematic transformations listed in Table II.

References

[1] R. Kaufmann, J. Pfaeffle, B. Blankenhorn, K. Stabile, D. Robertson, and R. Goitz, "Kinematics of the midcarpal and radiocarpal joints in radioulnar deviation: an in vitro study," *The Journal of hand surgery*, vol. 30, no. 5, pp. 937–942, 2005.

[2] R. A. Kaufmann, H. J. Pfaeffle, B. D. Blankenhorn, K. Stabile, D. Robertson, and R. Goitz, "Kinematics of the midcarpal and radiocarpal joint in flexion and extension: an in vitro study," *The Journal of hand surgery*, vol. 31, no. 7, pp. 1142–1148, 2006.

[3] M. J. Rainbow, R. N. Kamal, E. Leventhal, E. Akelman, D. C. Moore, S. W. Wolfe, and J. J. Crisco, "In vivo kinematics of the scaphoid, lunate, capitate, and third metacarpal in extreme wrist flexion and extension," *The Journal of hand surgery*, vol. 38, no. 2, pp. 278–288, 2013.

[4] D. C. Moore, J. J. Crisco, T. G. Trafton, and E. L. Leventhal, "A digital database of wrist bone anatomy and carpal kinematics," *Journal of biomechanics*, vol. 40, no. 11, pp. 2537–2542, 2007.

[5] B. Akhbari, D. C. Moore, D. H. Laidlaw, A.-P. C. Weiss, E. Akelman, S. W. Wolfe, and J. J. Crisco, "Predicting carpal bone kinematics using an expanded digital database of wrist carpal bone anatomy and kinematics," *Journal of Orthopaedic Research®*, 2019.

[6] P. Salvia, L. Woestyn, J. H. David, V. Feipel, S. Van, S. Jan, P. Klein, and M. Rooze, "Analysis of helical axes, pivot and envelope in active wrist circumduction," *Clinical Biomechanics*, vol. 15, no. 2, pp. 103–111, 2000.

[7] E. Biryukova, A. Roby-Brami, A. Frolov, and M. Mokhtari, "Kinematics of human arm reconstructed from spatial tracking system recordings," *Journal of biomechanics*, vol. 33, no. 8, pp. 985–995, 2000.

[8] C. G. Rose, C. K. Kann, A. D. Deshpande, and M. K. O'Malley, "Estimating anatomical wrist joint motion with a robotic exoskeleton," in *2017 International Conference on Rehabilitation Robotics (ICORR)*. IEEE, 2017, pp. 1437–1442.

[9] N. Yu and C. Xu, "An improved wrist kinematic model for human-robot interaction," *arXiv preprint arXiv:2002.05790*, 2020.

[10] Z.-M. Li, L. Kuxhaus, J. A. Fisk, and T. H. Christophel, "Coupling between wrist flexion-extension and radial-ulnar deviation," *Clinical biomechanics*, vol. 20, no. 2, pp. 177–183, 2005.

[11] S. K. Charles and N. Hogan, "Dynamics of wrist rotations," *Journal of biomechanics*, vol. 44, no. 4, pp. 614–621, 2011.

[12] D. Formica, S. K. Charles, L. Zollo, E. Guglielmelli, N. Hogan, and H. I. Krebs, "The passive stiffness of the wrist and forearm," *Journal of neurophysiology*, vol. 108, no. 4, pp. 1158–1166, 2012.

[13] M. Laitenberger, M. Raison, D. Périé, and M. Begon, "Refinement of the upper limb joint kinematics and dynamics using a subject-specific closed-loop forearm model," *Multibody System Dynamics*, vol. 33, no. 4, pp. 413–438, 2015.

[14] S. Duprey, A. Naaim, F. Moissenet, M. Begon, and L. Cheze, "Kinematic models of the upper limb joints for multibody kinematics optimisation: An overview," *Journal of biomechanics*, vol. 62, pp. 87–94, 2017.

[15] M. Esmaeili, K. Gamage, E. Tan, and D. Campolo, "Ergonomic considerations for anthropomorphic wrist exoskeletons: A simulation study on the effects of joint misalignment," in *2011 IEEE/RSJ International Conference on Intelligent Robots and Systems*. IEEE, 2011, pp. 4905–4910.

[16] J. Wang and O. Barry, "Multibody analysis and control of a full-wrist exoskeleton for tremor alleviation," *Journal of Biomechanical Engineering*, 2020.

[17] A. Gupta, M. K. O'Malley, V. Patoglu, and C. Burgar, "Design, control and performance of ricewrist: a force feedback wrist exoskeleton for rehabilitation and training," *The International Journal of Robotics Research*, vol. 27, no. 2, pp. 233–251, 2008.

[18] E. Pezent, C. G. Rose, A. D. Deshpande, and M. K. O'Malley, "Design and characterization of the openwrist: A robotic wrist exoskeleton for coordinated hand-wrist rehabilitation," in *2017 International Conference on Rehabilitation Robotics (ICORR)*. IEEE, 2017, pp. 720–725.

[19] R. C. Loureiro, J. M. Belda-Lois, E. R. Lima, J. L. Pons, J. J. Sanchez-Lacuesta, and W. S. Harwin, "Upper limb tremor suppression in adl via an orthosis incorporating a controllable double viscous beam actuator," in *9th International Conference on Rehabilitation Robotics, 2005. ICORR 2005.* Ieee, 2005, pp. 119–122.

[20] B. Taheri, "Real-time pathological tremor identification and suppression in human arm via active orthotic devices," Ph.D. dissertation, Southern Methodist University, 2013.

[21] L. V. Kalia and A. E. Lang, "Parkinson's disease," *The Lancet*, vol. 386, no. 9996, pp. 896 – 912, 2015. [Online]. Available: http://www.sciencedirect.com/science/article/pii/S0140673614613933

[22] J. Benito-Leon and E. D. Louis, "Essential tremor: emerging views of a common disorder," *Nature Reviews Neurology*, vol. 2, no. 12, p. 666, 2006.

[23] S. S. Haykin, *Adaptive filter theory*. Pearson Education India, 2005.

[24] E. A. Wan and A. T. Nelson, "Dual extended kalman filter methods," *Kalman filtering and neural networks*, vol. 123, 2001.

[25] A. P. L. Bo, P. Poignet, and C. Geny, "Pathological tremor and voluntary motion modeling and online estimation for active compensation," *IEEE Transactions on Neural Systems and Rehabilitation Engineering*, vol. 19, no. 2, pp. 177–185, 2010.

[26] K. C. Veluvolu and W. T. Ang, "Estimation of physiological tremor from accelerometers for real-time applications," *Sensors*, vol. 11, no. 3, pp. 3020–3036, 2011.

[27] V. Bonnet, C. Mazza, J. McCamley, and A. Cappozzo, "Use of weighted fourier linear combiner filters to estimate lower trunk 3d orientation from gyroscope sensors data," *Journal of neuroengineering and rehabilitation*, vol. 10, no. 1, pp. 1–8, 2013.

[28] S. Tatinati, K. C. Veluvolu, and W. T. Ang, "Multistep prediction of physiological tremor based on machine learning for robotics assisted microsurgery," *IEEE transactions on cybernetics*, vol. 45, no. 2, pp. 328–339, 2014.

[29] A. Y. Aravkin, J. V. Burke, and G. Pillonetto, "Optimization viewpoint on kalman smoothing with applications to robust and sparse estimation," in *Compressed sensing & sparse filtering*. Springer, 2014, pp. 237–280.

[30] A. S. Charles, A. Balavoine, and C. J. Rozell, "Dynamic filtering of time-varying sparse signals via l1 minimization," *IEEE Transactions on Signal Processing*, vol. 64, no. 21, pp. 5644–5656, 2016.

[31] J. Wang, S. K. Gupta, and O. Barry, "Modeling analysis of the wrist dynamics via an ellipsoidal joint." in *(To Appear) Dynamic Systems and Control Conference*. American Society of Mechanical Engineers, 2020.

[32] A. Seth, M. Sherman, P. Eastman, and S. Delp, "Minimal formulation of joint motion for biomechanisms," *Nonlinear dynamics*, vol. 62, no. 1-2, pp. 291–303, 2010.

[33] J. Diebel, "Representing attitude: Euler angles, unit quaternions, and rotation vectors," *Matrix*, vol. 58, no. 15-16, pp. 1–35, 2006.

[34] R. V. Gonzalez, T. S. Buchanan, and S. L. Delp, "How muscle architecture and moment arms affect wrist flexion-extension moments," *Journal of biomechanics*, vol. 30, no. 7, pp. 705–712, 1997.

[35] K. R. Holzbaur, W. M. Murray, and S. L. Delp, "A model of the upper extremity for simulating musculoskeletal surgery and analyzing neuromuscular control," *Annals of biomedical engineering*, vol. 33, no. 6, pp. 829–840, 2005.

[36] E. A. Wan and R. Van Der Merwe, "The unscented kalman filter for nonlinear estimation," in *Proceedings of the IEEE 2000 Adaptive Systems for Signal Processing, Communications, and Control Symposium (Cat. No. 00EX373)*. Ieee, 2000, pp. 153–158.

[37] C. E. Clauser, J. T. McConville, and J. W. Young, "Weight, volume, and center of mass of segments of the human body," Antioch Coll Yellow Springs OH, Tech. Rep., 1969.

[38] H. P. Singh, J. J. Dias, H. Slijper, and S. Hovius, "Assessment of velocity, range, and smoothness of wrist circumduction using flexible electrogoniometry," *The Journal of hand surgery*, vol. 37, no. 11, pp. 2331–2339, 2012.

[39] J. J. Crisco, W. M. Heard, R. R. Rich, D. J. Paller, and S. W. Wolfe, "The mechanical axes of the wrist are oriented obliquely to the anatomical axes," *The Journal of Bone and Joint Surgery. American volume.*, vol. 93, no. 2, p. 169, 2011.

[40] A. Leardini, L. Chiari, U. Della Croce, and A. Cappozzo, "Human movement analysis using stereophotogrammetry: Part 3. soft tissue artifact assessment and compensation," *Gait & posture*, vol. 21, no. 2, pp. 212–225, 2005.

[41] V. Sholukha, B. Bonnechere, P. Salvia, F. Moiseev, M. Rooze, and S. V. S. Jan, "Model-based approach for human kinematics reconstruction from markerless and marker-based motion analysis systems," *Journal of biomechanics*, vol. 46, no. 14, pp. 2363–2371, 2013.

[42] S. O. Madgwick, A. J. Harrison, and R. Vaidyanathan, "Estimation of imu and marg orientation using a gradient descent algorithm," in *2011 IEEE international conference on rehabilitation robotics*. IEEE, 2011, pp. 1–7.